

A full Eulerian finite difference approach for solving fluid-structure coupling problems

Kazuyasu Sugiyama¹, Satoshi Ii¹, Shintaro Takeuchi¹, Shu Takagi^{2,1} & Yoichiro Matsumoto¹

¹ Department of Mechanical Engineering, School of Engineering, The University of Tokyo,
7-3-1 Hongo Bunkyo-Ku, Tokyo 113-8656, Japan

² Organ and Body Scale Team, CSRP, Riken, 2-1, Hirosawa, Wako-shi, Saitama 351-0198, Japan

A new simulation method for solving fluid-structure coupling problems has been developed. All the basic equations are numerically solved on a fixed Cartesian grid using a finite difference scheme. A volume-of-fluid formulation (Hirt & Nichols (1981, *J. Comput. Phys.*, **39**, 201)), which has been widely used for multiphase flow simulations, is applied to describing the multi-component geometry. The temporal change in the solid deformation is described in the Eulerian frame by updating a left Cauchy-Green deformation tensor, which is used to express constitutive equations for nonlinear Mooney-Rivlin materials. In this paper, various verifications and validations of the present full Eulerian method, which solves the fluid and solid motions on a fixed grid, are demonstrated, and the numerical accuracy involved in the fluid-structure coupling problems is examined.

PACS numbers: 47.11.Bc, 47.10.A-, 47.55.-t

I. INTRODUCTION

Fluid-Structure Interaction (FSI) phenomena appear in many places, e.g., biological systems, and industrial processes. In life science, the numerical prediction of the FSI problems involves twofold significance: fundamental and practical aspects. For example, it would allow us to gain insight into how life is sustained, and support surgical planning in medical treatments. Conventionally, the computational fluid dynamics is modelled in an Eulerian way, while the computational structure dynamics is normally treated in a Lagrangian way. The coupling of the fluid and structure dynamics is a formidable task due to such a difference in the numerical framework as well as its multi-physics nature.

In a creeping (zero Reynolds number limit) flow involving a biological membrane, once boundary conditions on the membrane surface are determined via constitutive laws for e.g. an in-plane stress and a bending moment, the bulk flow field is found using Green's function. In such a situation, no volumetric mesh is needed in the bulk region. A boundary element method is applicable to predicting capsule [59] and red blood cell [60] motions interacting with the fluid flow.

For non-zero Reynolds number flows, on the other hand, it is necessary to set out the computational mesh over the entire domain. There are currently several major approaches classified with respect to the computational treatment how the kinematic and dynamic interactions are coupled on the moving interface.

The most accurate approach is raised as Arbitrary Lagrangian Eulerian (ALE) [3, 22, 29, 30, 50] or Deforming-Spatial-Domain/Space-Time (DSD/ST) [31, 75, 76] technique, in which the body-fitted mesh is used. The latter method enables one to arbitrarily choose spatiotemporal nodes, and facilitates to simulate the moving particle and FSI problems. These approaches are referred to as an interface-tracking approach, in which the surface mesh is accommodated to be shared between both the fluid and solid phases, and thus to automatically satisfy the kinematic condition. As the flow is resolved along the moving/deforming object surface, the boundary layer is expected to be highly resolved, and the dynamic interaction is accurately coupled through iterative procedures. Once the body-fitted mesh is provided, the state-of-the-art of the interface-tracking approach is satisfactory for achieving accurate predictions, including the applications of moving rigid particles [25, 37], moving hyperelastic particles [12], parachute aerodynamics [68], blood flows [2, 11, 74, 77–79] and heart flows [84, 95]. However, the whole computational domain has to be re-meshed as the object moves/deforms, which is computationally expensive.

An alternative to the interface-tracking approach is an Eulerian-Lagrangian approach, in which the fluid and solid phases are separately formulated on the fixed Eulerian and Lagrangian grids, respectively. A noticeable contribution is the development of the Immersed Boundary (IB) method by Peskin [57, 58], who introduces a pseudo delta function for communication between the Eulerian and Lagrangian quantities, and demonstrated the landmark simulation of the blood flow around heart valves [57, 58]. The Fictitious Domain (FD) method [14, 15, 65, 90], and PHYSALIS [71, 96] for specific multiphase flow problems with circular or spherical particle are also classified into the Eulerian-Lagrangian approach. The IB and FD methods have been applied to a variety of studies, for example, moving rigid particles [14, 15, 39, 40, 91], moving flexible bodies [27, 49, 97], red blood cell motion [10, 16, 49], and restricted diffusion with permeable interfaces [26]. The IB method has also inspired many researchers to propose a number of improved methods. For example, to facilitate the application to medical problems, the immersed finite element method, in which a new kernel function instead of the pseudo delta function is introduced for determining the cut-off region around the

interface on a non-uniform mesh system, is proposed in [44, 92–94]. Also, the immersed interface treatment [41–43, 73] improves the sharpness of the interface by incorporating the jump in the stress and velocities across the interface. Recently, a conservative momentum exchange method [72] is proposed to facilitate the simulation of the fluid flow involving a number of elastic particles by combining the finite difference and finite element approaches.

In the above-mentioned methods for predicting the motion/deformation of hyperelastic material, the solid displacement is temporally updated in the Lagrangian way. In general, the hyperelastic constitutive law is expressed as a function of the deformation gradient tensor $\mathbf{F} = \partial \mathbf{x} / \partial \mathbf{X}$, here \mathbf{x} denotes the current coordinates, and \mathbf{X} the reference coordinates [4]. The label of each Lagrangian node links the reference configuration and the set of the current node positions representing the current configuration. Therefore, the Lagrangian description has been preferably employed. However, the re-meshing procedure at each time step leads to intensive computation if system involves complicated geometry of solid and/or a large number of objects [69].

Let us consider patient-specific simulations in a medical field. The multi-component geometry of the inner side of the human body is provided as voxel data, which are converted from the medical image of a Computed Tomography (CT) or a Magnetic Resonance Imaging (MRI). The basic idea of the medical image-based simulation is found in [74, 77], in which the voxel data are converted into the finite element mesh before starting the computation, and the mesh is reconstructed with time advancement. As pointed out in [47, 51, 88], since technical knowledge and expertise are required for the mesh generation and reconstruction, an alternative simulation method without mesh generation procedure would be desirable to extend the FSI simulation to certain additional classes of problems in the medical field. Motivated by such a practical background, the full Eulerian finite difference methods, which directly access the voxel data to describe the *rigid* boundary on the fixed Cartesian mesh and avoid difficulty in mesh generation and reconstruction, have been developed in [47, 88]. The application includes the prediction of a coil embolization for aneurysms [51], which has been used in practice to support surgical planning.

We further develop a full Eulerian method for fluid-structure interactions involving flexible hyperelastic material. In the interface-capturing methods for multiphase flow simulations, for instance, Volume-Of-Fluid (VOF) [23], level set [6, 55, 56, 64, 70], and phase field [35, 85] approaches, one set of governing equations for the whole flow field, referred to as a one-fluid formulation [81], is often employed. We follow such an idea, and write all the basic equations on a fixed Cartesian grid in a finite difference form. Several Eulerian solvers for modelling the solid deformation have been proposed for linear elastic materials [47, 87], for elasto-plastic materials [54, 82] for neo-Hookean materials [9, 46, 83] and for more general hyperelastic materials [8]. We treat a Mooney-Rivlin hyperelastic material [48, 61], and consider the nonlinearity of the Cauchy stress with respect to a left Cauchy-Green deformation tensor [4, 20]. Our fluid-structure coupling approach is characterized by the feasibility in implementing the hyperelastic constitutive law into the standard incompressible fluid flow solvers, and also by the treatments in capturing the fluid-structure interface and the solid deformation. In the Lagrangian method, the body-fit finite elements automatically distinguish between the fluid and solid phases. In the present Eulerian method, considering that the voxel data contain the volume fraction of fluid and solid, we apply the VOF formulation [23] to describing the multi-component geometry (see figure 1). The large deformation is usually described by using the Piola-Kirchhoff stress tensor as a function of the deformation gradient, which is suited to the Lagrangian formulation as mentioned above. By contrast, the Eulerian formulation lacks of the material points to link between the reference and current configurations. Therefore, we must devise a method to quantify the level of deformation. To this end, we introduce the left Cauchy-Green deformation tensor $\mathbf{B}(= \mathbf{F} \cdot \mathbf{F}^T)$ defined on each grid point, and temporally update it (see figure 2). We will devote several test computations to the verification and validation, and investigate the numerical accuracy involved in the fluid-structure coupling.

The paper is organized as follows. In §II, we present the details of the basic equations of the system consisting of Newtonian fluid and hyperelastic material, and formulate constitutive equations suited to the full Eulerian FSI simulation. In §III, we explain the simulation methods in terms of the time-stepping algorithm and the finite difference descriptions. In §IV, to explore the validity of the advocated numerical procedure, we perform three kinds of tests. Firstly, we address a one-dimensional problem of the oscillatory parallel fluid-solid layers. Secondly, we make comparisons with available simulations. Thirdly, we examine how the shape reversibility of the hyperelastic materials is reproduced. In §V, we provide some perspectives to conclude the paper.

II. BASIC EQUATIONS

A. Governing equations and fluid-structure mixture representations

Figure 3 shows the notation of the fluid-structure systems to be addressed. Let us consider an incompressible hyperelastic domain Ω_s submerged in an incompressible fluid domain Ω_f , which is bounded with rigid flat walls. Hereafter, the suffices f and s stand for the fluid and solid phases, respectively. We focus on the system, where the

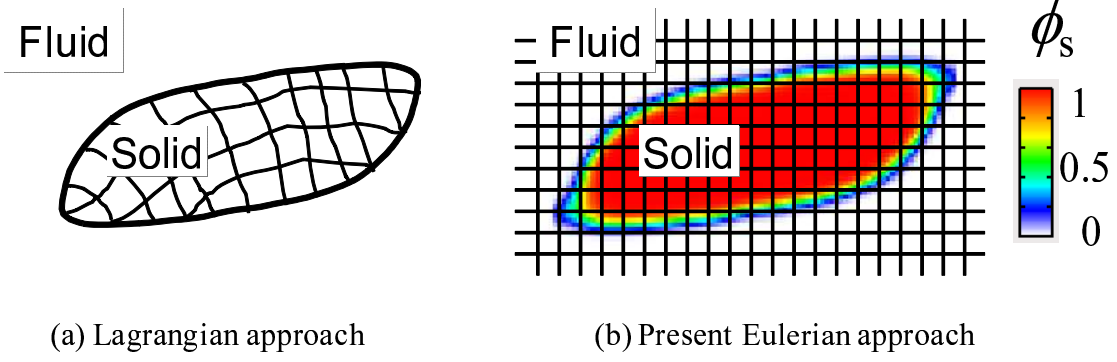


FIG. 1: Schematic figure explaining the difference between the interface recognitions of the Lagrangian and Eulerian approaches. In the Lagrangian method, the body-fit mesh distinguishes between fluid and solid phases, while in the present Eulerian method, the solid volume fraction ϕ_s does. The contour at $\phi_s = 1/2$ indicates the interface.

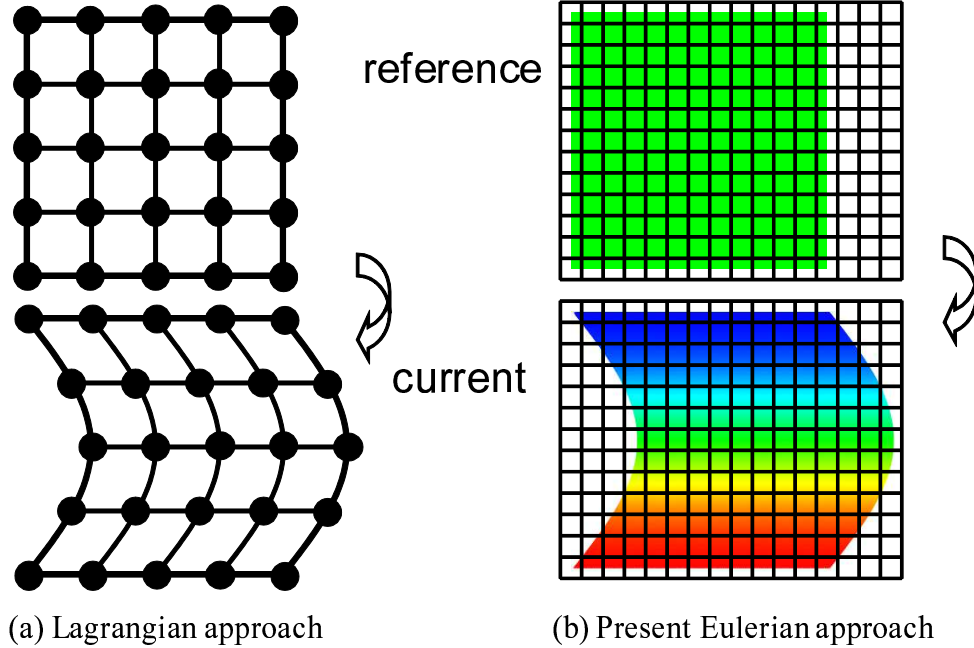


FIG. 2: Schematic figure explaining the difference between the solid deformation descriptions of the Lagrangian and Eulerian approaches. In the Lagrangian method, the relative displacement between adjacent material points from the reference to current configurations quantifies the deformation level. In the present Eulerian method, to quantify the deformation, the left Cauchy-Green deformation tensor \mathbf{B} is introduced in the Eulerian frame, and temporally updated.

walls are in contact with only fluid at the boundary Γ_W , and the moving wall drives the fluid and solid motions. Both fluid and solid are homogeneous, i.e., the material properties are uniform inside each phase. We shall restrict our attention to the kinematic and dynamic interactions at the fluid-structure interface Γ_I . The fluid and solid densities are assumed to be identical ($\rho_f = \rho_s = \rho$) as in many analyses for biological systems (e.g. [79, 97]), and no external body force ($\mathbf{b} = 0$) is to be exerted on the continua. The extensions to the non-identical density and the non-zero body force would be readily achieved.

For incompressible fluid and solid, the governing equations consist of the mass and momentum conservations:

$$\begin{aligned} \nabla \cdot \mathbf{v}_f &= 0, & \mathbf{x} \in \Omega_f, \\ \nabla \cdot \mathbf{v}_s &= 0, & \mathbf{x} \in \Omega_s, \end{aligned} \tag{1}$$

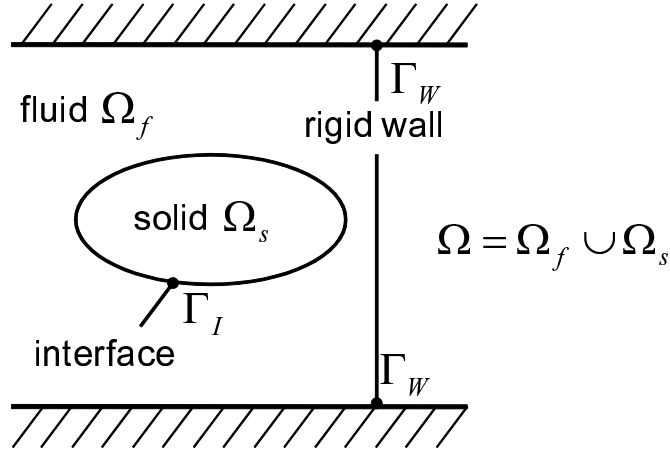


FIG. 3: Abstract setting for the FSI problem considered in the present study.

$$\begin{aligned} \rho(\partial_t \mathbf{v}_f + \mathbf{v}_f \cdot \nabla \mathbf{v}_f) &= \nabla \cdot \boldsymbol{\sigma}_f, & \mathbf{x} \in \Omega_f, \\ \rho(\partial_t \mathbf{v}_s + \mathbf{v}_s \cdot \nabla \mathbf{v}_s) &= \nabla \cdot \boldsymbol{\sigma}_s, & \mathbf{x} \in \Omega_s, \end{aligned} \quad (2)$$

where \mathbf{v} denotes the velocity vector, t the time, ρ the density, and $\boldsymbol{\sigma}$ the Cauchy stress tensor.

The no-slip condition is imposed on the fluid-wall boundary, namely

$$\mathbf{v}_f = \mathbf{V}_W, \quad \mathbf{x} \in \Gamma_W, \quad (3)$$

where \mathbf{V}_W denotes the wall velocity. The kinematic and dynamic interactions between the fluid and solid phases are determined by continuity in the velocity and in the traction force at the fluid-structure interface, namely,

$$\mathbf{v}_f = \mathbf{v}_s, \quad \mathbf{x} \in \Gamma_I, \quad (4)$$

$$\boldsymbol{\sigma}_f \cdot \mathbf{n} = \boldsymbol{\sigma}_s \cdot \mathbf{n}, \quad \mathbf{x} \in \Gamma_I, \quad (5)$$

where \mathbf{n} denotes the unit normal vector at the interface.

In the practical numerical procedure based on the full Eulerian perspective, instead of separately partitioned two velocity fields \mathbf{v}_f and \mathbf{v}_s respectively in Ω_f and in Ω_s , it is convenient to introduce a monolithic velocity vector \mathbf{v} applied to the entire domain $\Omega (= \Omega_f \cup \Omega_s)$. In multiphase flow simulations, one set of governing equations for the whole flow field, known as a one-fluid formulation [81], is often employed to be discretized on a fixed grid. In the present study, such an idea is applied to the fluid-structure system by using \mathbf{v} , that is here referred to as a *one-continuum* formulation. The one-continuum formulation would immediately satisfy (4) because \mathbf{v} is supposed to be continuous across the interface Γ_I . Following the volume-averaging procedure [72], we establish the velocity field \mathbf{v} as

$$\mathbf{v} = (1 - \phi_s) \mathbf{v}_f + \phi_s \mathbf{v}_s, \quad (6)$$

where ϕ_s is the volume fraction of solid inside a computational cell:

$$\phi_s(x, y, z) = \frac{1}{\Delta_x \Delta_y \Delta_z} \int_{-\Delta_x/2}^{\Delta_x/2} d\hat{x} \int_{-\Delta_y/2}^{\Delta_y/2} d\hat{y} \int_{-\Delta_z/2}^{\Delta_z/2} d\hat{z} I_s(x + \hat{x}, y + \hat{y}, z + \hat{z}), \quad (7)$$

where Δ denotes the grid size, the suffices x, y and z stand for the respective directions, and I_s the indicator function defined by

$$I_s(\mathbf{x}) = \begin{cases} 1 & \text{for } \mathbf{x} \in \Omega_s, \\ 0 & \text{for } \mathbf{x} \in \Omega_f. \end{cases} \quad (8)$$

We may regard the volume fraction ϕ_s as a smoothed Heaviside function at the grid scale. The distribution of the volume fraction reveals $\phi_s = 0$ in fluid, $\phi_s = 1$ in solid, and $0 < \phi_s < 1$ for the grid involving the fluid-solid interface. As explained in §IV B 1, the modulus of its gradient $|\nabla \phi_s|$ is regarded as a smoothed one-dimensional delta function

at the grid scale Δ_x . Namely, for the grid involving only fluid or solid, $|\nabla\phi_s|$ is zero, whereas for the grid involving the interface, $|\nabla\phi_s|$ reveals a peak of the order of Δ_x^{-1} . The isoline at $\phi_s = 1/2$ represents the interface Γ_I (see figure 1(b)). In several approaches for multiphase flow simulations (e.g., VOF [23] and level set [6, 70] methods), the viscous stress is often written in a mixture form: i.e., the smoothed Heaviside function H smears out the viscosity such as $\mu_{\text{mix}} = (1 - H)\mu_1 + H\mu_2$ to remove the discontinuity of the stress across the interface Γ_I . The mixture representation is employed in the present study. For incompressible continua, the pressure p may be regarded as of a Lagrangian multiplier imposing the solenoidal condition over the whole velocity field. The Poisson equation will be solved to find the pressure field p , written in the one-continuum form, over the entire domain Ω . Taking the weighted average with respect to ϕ_s , we write the mixture stress $\boldsymbol{\sigma}$ as

$$\boldsymbol{\sigma} = -p\mathbf{I} + (1 - \phi_s)\boldsymbol{\sigma}'_f + \phi_s\boldsymbol{\sigma}'_s, \quad \mathbf{x} \in \Omega, \quad (9)$$

where \mathbf{I} denotes the unit tensor, and the prime on the second-order tensor stands for the deviatoric tensor, e.g. $\mathbf{T}' = \mathbf{T} - \frac{1}{3}\text{tr}(\mathbf{T})\mathbf{I}$ for a tensor \mathbf{T} . Since ϕ_s is smoothed at the grid scale and $\boldsymbol{\sigma}$ is supposed to be smoothly distributed over the entire domain, the expression (9) at $\phi_s = 1/2$ would satisfy the continuity of the traction force (5). To advect the scalar field ϕ_s , the purely Eulerian interface method is employed. Throughout the paper, the fluid component is assumed to be Newtonian, and thus the deviatoric stress of fluid is given by

$$\boldsymbol{\sigma}'_f = 2\mu_f\mathbf{D}', \quad (10)$$

where μ_f denotes the dynamic viscosity of fluid, and $\mathbf{D} (= \frac{1}{2}(\nabla\mathbf{v} + \nabla\mathbf{v}^T))$ the strain rate tensor. Instead of (1) and (2) with (4), (5) and (9), we solve the following equations in the one-continuum form over the entire domain:

$$\nabla \cdot \mathbf{v} = 0, \quad \mathbf{x} \in \Omega, \quad (11)$$

$$\rho(\partial_t\mathbf{v} + \mathbf{v} \cdot \nabla\mathbf{v}) = -\nabla p + \nabla \cdot \{2(1 - \phi_s)\mu_f\mathbf{D}' + \phi_s\boldsymbol{\sigma}'_s\}, \quad \mathbf{x} \in \Omega, \quad (12)$$

$$\partial_t\phi_s + \mathbf{v} \cdot \nabla\phi_s = 0, \quad \mathbf{x} \in \Omega. \quad (13)$$

The deviatoric stress $\boldsymbol{\sigma}'_s$ of solid is dependent on the constitutive law. The incompressible Mooney-Rivlin law [20, 48, 61] involving a nonlinearity with respect to \mathbf{B} (here $\mathbf{B} = \mathbf{F} \cdot \mathbf{F}^T$ denotes the left Cauchy-Green deformation tensor, $\mathbf{F} = \partial\mathbf{x}/\partial\mathbf{X}$ the deformation gradient, \mathbf{x} the current coordinates, and \mathbf{X} the reference coordinates [4]) is incorporated into the finite difference method. The constitutive equations and the solution algorithm will be presented in the following sections.

B. Constitutive equations for solid

In most of finite element computations, the constitutive equations of hyperelastic material are written over the reference configuration. The hyperelastic constitutive law is usually provided by using the first or second Piola-Kirchhoff stress tensor, which is differentiated with respect to the reference coordinates \mathbf{X} in the momentum equation. It is suited to the Lagrangian frame. By contrast, in the Eulerian approach, the equation set is written over the current configuration. Therefore, the constitutive equations are needed to be temporally updated on the fixed grid without using the Lagrangian mesh. In this section, we describe the constitutive law in the Cauchy stress form, and the transport of the left Cauchy-Green deformation tensor field, which are the core elements of the present approach.

1. Cauchy stress expression of the incompressible Mooney-Rivlin law involving nonlinearity up to $O(\mathbf{B}^2)$

We consider incompressible visco-hyperelastic materials undergoing only the isochoric motion. The deviatoric Cauchy stress of solid is expressed as

$$\boldsymbol{\sigma}'_s = 2\mu_s\mathbf{D}' + \boldsymbol{\sigma}'_{sh}, \quad (14)$$

where the first term on the right-hand-side corresponds to the viscous contribution with dynamic viscosity μ_s . The second term $\boldsymbol{\sigma}'_{sh}$ corresponds to the hyperelastic contribution to be derived below.

To formulate the constitutive equation, we refer to the general theories [19, 66, 80] of constrained material. Choosing the Mooney-Rivlin expression [48, 61], and considering the nonlinearity up to $O(\mathbf{B}^2)$ in the deviatoric Cauchy stress, we write the hyperelastic strain energy potential W as

$$W = c_1(\tilde{\text{I}}_C - 3) + c_2(\tilde{\text{II}}_C - 3) + c_3(\tilde{\text{I}}_C - 3)^2, \quad (15)$$

where $\tilde{\text{I}}_C$ and $\tilde{\text{II}}_C$ denote reduced invariants [20] of the right Cauchy-Green deformation tensor $\mathbf{C} = \mathbf{F}^T \cdot \mathbf{F}$ defined by

$$\tilde{\text{I}}_C = \frac{\text{I}_C}{\text{III}_C^{1/3}}, \quad \tilde{\text{II}}_C = \frac{\text{II}_C}{\text{III}_C^{2/3}}, \quad (16)$$

where

$$\text{I}_C = \text{tr}(\mathbf{C}), \quad \text{II}_C = \frac{1}{2}\{\text{I}_C^2 - \text{tr}(\mathbf{C} \cdot \mathbf{C})\}, \quad \text{III}_C = \det(\mathbf{C}).$$

Utilizing the equivalence of the invariants between the left and right Cauchy-Green deformation tensors [24], we write the deviatoric Cauchy stress tensor as

$$\begin{aligned} \boldsymbol{\sigma}'_{sh} &= \frac{1}{\det(\mathbf{F})} \mathbf{F} \cdot \left\{ 2 \frac{\partial W}{\partial \text{I}_C} \frac{\partial \text{I}_C}{\partial \mathbf{C}} + 2 \frac{\partial W}{\partial \text{II}_C} \frac{\partial \text{II}_C}{\partial \mathbf{C}} + 2 \frac{\partial W}{\partial \text{III}_C} \frac{\partial \text{III}_C}{\partial \mathbf{C}} \right\} \cdot \mathbf{F}^T \\ &= (2c_1 \mathbf{B} + 2c_2(\text{tr}(\mathbf{B})\mathbf{B} - \mathbf{B} \cdot \mathbf{B}) + 4c_3(\text{tr}(\mathbf{B}) - 3)\mathbf{B})'. \end{aligned} \quad (17)$$

We will give several demonstrations afterward for some specific cases based on the linear Mooney-Rivlin, neo-Hookean, and incompressible Saint Venant-Kirchhoff materials. Note that all these materials obey (17). For *linear* Mooney-Rivlin material ($c_3 = 0$) [24, 48, 61], which is often used as the biological material, Cauchy stress becomes

$$\boldsymbol{\sigma}'_{sh} = 2c_1 \mathbf{B}' + 2c_2(\text{tr}(\mathbf{B})\mathbf{B} - \mathbf{B} \cdot \mathbf{B})'. \quad (18)$$

The neo-Hookean material is a particular case of the linear Mooney-Rivlin material with the coefficients

$$c_1 = \frac{G}{2}, \quad c_2 = c_3 = 0,$$

where G denotes the modulus of transverse elasticity. The corresponding Cauchy stress is

$$\boldsymbol{\sigma}'_{sh} = G\mathbf{B}'. \quad (19)$$

As another typical hyperelastic material, we consider Saint Venant-Kirchhoff material [4, 13, 63], which often models a thin but finite volume membrane. The constitutive equation is expressed as a simple extension of Hooke's law, as defined by

$$\mathbf{S} = \lambda_{\text{Lamé}}^s \text{tr}(\mathbf{E})\mathbf{I} + 2\mu_{\text{Lamé}}^s \mathbf{E},$$

where \mathbf{S} is the second Piola-Kirchhoff stress, $\lambda_{\text{Lamé}}^s$, $\mu_{\text{Lamé}}^s$ are the Lamé constants, and $\mathbf{E} = \frac{1}{2}(\mathbf{C} - \mathbf{I})$ is the Green-Lagrange strain tensor. Although the Saint Venant-Kirchhoff material is usually referred to as dilatable, we implement the *incompressible* Saint Venant-Kirchhoff model, as defined in [18]. The deviatoric Cauchy stress of the incompressible Saint Venant-Kirchhoff material is expressed as

$$\boldsymbol{\sigma}'_{sh} = \left(\frac{\mathbf{F} \cdot \mathbf{S} \cdot \mathbf{F}^T}{\det(\mathbf{F})} \right)' = \frac{\lambda_{\text{Lamé}}^s}{2}(\text{tr}(\mathbf{B}) - 3)\mathbf{B}' + \mu_{\text{Lamé}}^s(\mathbf{B} \cdot \mathbf{B} - \mathbf{B})'. \quad (20)$$

Substituting the relations

$$c_1 = \mu_{\text{Lamé}}^s, \quad c_2 = -\frac{\mu_{\text{Lamé}}^s}{2}, \quad c_3 = \frac{\lambda_{\text{Lamé}}^s + 2\mu_{\text{Lamé}}^s}{8},$$

into (17), we can readily realize that the constitutive law (20) falls within the class of nonlinear Mooney-Rivlin laws.

2. Transport of left Cauchy-Green deformation tensor field in the Eulerian frame

Once the coefficients c_1 , c_2 and c_3 are given, the constitutive equation (17) is expressed as a function of the left Cauchy-Green deformation tensor \mathbf{B} . If the tensor field \mathbf{B} is determined in a purely Eulerian manner, all the equations will be closed in the Eulerian form. Utilizing the fact that the upper convected time derivative of \mathbf{B} is identically zero [4], one may use the following transport equation to update the \mathbf{B} field:

$$\partial_t \mathbf{B} + \mathbf{v} \cdot \nabla \mathbf{B} = \mathbf{L} \cdot \mathbf{B} + \mathbf{B} \cdot \mathbf{L}^T, \quad (21)$$

where $\mathbf{L} (= (\nabla \mathbf{v})^T)$ denotes the velocity gradient tensor. For the initially unstressed solid, the initial condition is given by $\mathbf{B} = \mathbf{I}$. It should be noticed that, however, it is quite cumbersome to solve (21) from a numerical viewpoint, because \mathbf{B} exhibits rough distribution in the fluid domain Ω_f [46]. The fluid element subject to a shearing motion is likely to elongate toward the extensional direction. Such an elongation causes a temporally exponential growth of some components of \mathbf{B} . To avoid the numerical instability brought by the exponential growth, instead of \mathbf{B} , we update the *modified* left Cauchy-Green deformation tensor $\tilde{\mathbf{B}} = \phi_s^\alpha \mathbf{B}$ ($\alpha > 0$), which yields

$$\partial_t \tilde{\mathbf{B}} + \mathbf{v} \cdot \nabla \tilde{\mathbf{B}} = \mathbf{L} \cdot \tilde{\mathbf{B}} + \tilde{\mathbf{B}} \cdot \mathbf{L}^T, \quad (22)$$

with the initial condition $\tilde{\mathbf{B}} = \phi_s^\alpha \mathbf{I}$. Because of $\tilde{\mathbf{B}} = 0$ for $\phi_s = 0$, the numerical instability is evaded in the fluid domain Ω_f . In the hyperelastic constitutive law (18), we consider the term up to $O(\mathbf{B}^2)$, of which the contribution to the phase averaged stress $\phi_s \boldsymbol{\sigma}_s$ in (9) is proportional to $\phi_s \mathbf{B}^2 = \phi_s^{1-2\alpha} \tilde{\mathbf{B}}^2$. In order to avoid division by zero in the fluid region $\phi_s = 0$, the exponent $1 - 2\alpha$ on ϕ_s should be non-negative, indicating $\alpha \leq 1/2$. In the present study, we choose the largest value $\alpha = 1/2$. Further, to avoid the inevitable exponential growth at the cell near the interface Γ_I containing the fluid-solid mixture, and to obtain a viable compromise between the numerical consistency and stability, we introduce a threshold ϕ_{\min} and enforce $\tilde{\mathbf{B}} = 0$ where $\phi_s < \phi_{\min}$. In the present study, we set ϕ_{\min} between 0.01 and 0.1.

3. Characteristics of the present approach in treating the solid stress

From (17), the resulting deviatoric stress of solid multiplied by ϕ_s , which is involved in (12), is expressed as

$$\begin{aligned} \phi_s \boldsymbol{\sigma}'_s = & 2\phi_s \mu_s \mathbf{D}' + (2c_1 \phi_s^{1/2} \tilde{\mathbf{B}} \\ & + 2c_2 (\text{tr}(\tilde{\mathbf{B}}) \tilde{\mathbf{B}} - \tilde{\mathbf{B}} \cdot \tilde{\mathbf{B}}) + 4c_3 (\text{tr}(\tilde{\mathbf{B}}) - 3\phi_s^{1/2}) \tilde{\mathbf{B}})' \end{aligned} \quad (23)$$

which can be evaluated together with the temporally updated $\tilde{\mathbf{B}}$ from (22).

It should be noted that when the material points are tracked in the Lagrangian way, the relation (21) is identically satisfied via the change in the relative position of the adjacent material points (see figure 2(a)). Thus, in the pure Lagrangian approach, it is not necessary to introduce a transport equation describing the deformation level such as \mathbf{B} . On the other hand, in the Eulerian approach, which does not rely on the material point, we must introduce the deformation level on the fixed mesh. The present approach is characterized by the introduction of the transport equation of $\tilde{\mathbf{B}}$, which is temporally updated in the Eulerian frame (see figure 2(b)).

III. SIMULATION METHODS

A. Overview

Once the initial field of the solid volume fraction ϕ_{s0} is given over the entire domain Ω , the present Eulerian method enables one to carry out the FSI simulation without mesh generation procedure. In order to prescribe the ϕ_{s0} field, it is only required to numerically compute the ratio of the occupied solid to each control volume from the initial geometry as a preprocess. If the system is initially at rest and unstressed, one can launch the simulation by setting the initial conditions of the velocity vector, pressure, and modified left Cauchy-Green deformation tensor to $\mathbf{v} = 0$, $p = 0$, and $\tilde{\mathbf{B}} = \phi_s^{1/2} \mathbf{I}$, respectively.

Instead of the *deviatoric* stress $\boldsymbol{\sigma}'$ (with a prime), we may use the following *pseudo* stress to make some discretized expressions for the individual stress components simple:

$$\tilde{\boldsymbol{\sigma}} = (\mu_f + (\mu_s - \mu_f) \phi_s) (\nabla \mathbf{v} + \nabla \mathbf{v}^T) + \phi_s \tilde{\boldsymbol{\sigma}}_{sh}, \quad (24)$$

where

$$\phi_s \tilde{\sigma}_{sh} = 2c_1 \phi_s^{1/2} \tilde{\mathbf{B}} + 2c_2 (\text{tr}(\tilde{\mathbf{B}}) \tilde{\mathbf{B}} - \tilde{\mathbf{B}} \cdot \tilde{\mathbf{B}}) + 4c_3 (\text{tr}(\tilde{\mathbf{B}}) - 3\phi_s^{1/2}) \tilde{\mathbf{B}}. \quad (25)$$

Introducing a *pseudo* pressure \tilde{p} , instead of (12), we solve

$$\rho (\partial_t \mathbf{v} + \mathbf{v} \cdot \nabla \mathbf{v}) = -\nabla \tilde{p} + \nabla \cdot \tilde{\boldsymbol{\sigma}}. \quad (26)$$

The actual pressure and deviatoric stress read

$$p = \tilde{p} - \frac{\text{tr}(\tilde{\boldsymbol{\sigma}})}{3}, \quad \boldsymbol{\sigma}' = \tilde{\boldsymbol{\sigma}} - \frac{\text{tr}(\tilde{\boldsymbol{\sigma}})}{3} \mathbf{I}.$$

Hereafter, the formulation will be given on the two-dimensional (2D) system. The extension to the three-dimensional (3D) system is straightforward [69]. The basic equations (11), (12), (13), (22) and (23) are solved by a finite difference method on a fixed Cartesian grid. The quantities \mathbf{v} , p , ϕ_s , and $\tilde{\mathbf{B}}$ are temporally updated in the Eulerian frame. The entire domain is discretized by a uniform square mesh. We follow a conventional staggered Marker-And-Cell (MAC) cell arrangement [21], where the velocity component is located on the cell face, and the pressure at the cell center (see figure 4(a)). The symmetry in the tensor $\tilde{\mathbf{B}}$ and the two-dimensionality of the system imply $\tilde{B}_{zz} = \phi_s^\alpha$, $\tilde{B}_{xz} = \tilde{B}_{zx} = \tilde{B}_{yz} = \tilde{B}_{zy} = 0$, and $\tilde{B}_{yx} = \tilde{B}_{xy}$. Hence, (22) is solved for the three independent components \tilde{B}_{xx} , \tilde{B}_{yy} and \tilde{B}_{xy} . The diagonal components of $\tilde{\mathbf{B}}$ and the solid volume fraction ϕ_s are defined on the cell center, while the non-diagonal components of $\tilde{\mathbf{B}}$ are on the cell apex (see figure 4(b)).

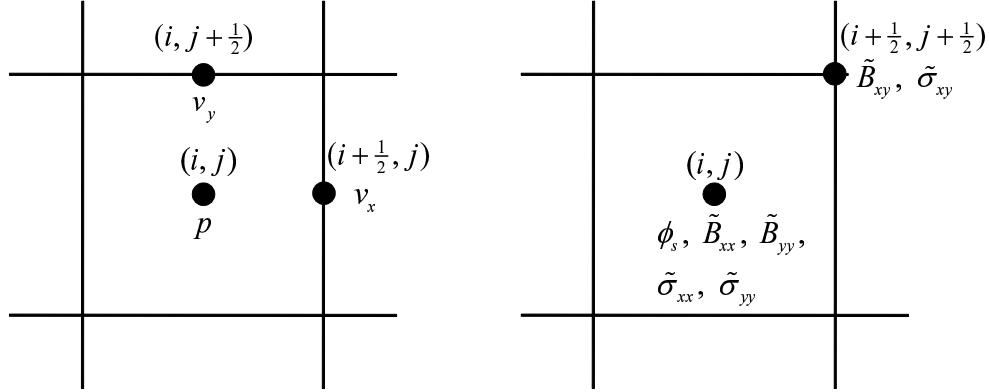


FIG. 4: Schematic figure of computational grid with the mesh size of $\Delta_x \times \Delta_y$, here $\Delta_x = \Delta_y$. (a) left panel: Definition points of the velocity components v_x , v_y , and the pressure p . (b) right panel: Definition points of the solid volume fraction ϕ_s , the stress components $\tilde{\sigma}_{xx}$, $\tilde{\sigma}_{yy}$, $\tilde{\sigma}_{xy}$, and the modified left Cauchy-Green deformation components \tilde{B}_{xx} , \tilde{B}_{yy} , \tilde{B}_{xy} .

As opposed to usual methods of computational structure dynamics, for instance, the GMRES approach [62] and the weak compressibility approach [7, 28], the pressure Poisson equation is solved to exactly satisfy the solenoidal condition (11) over the entire domain Ω likewise widely-used incompressible fluid flow algorithms. In solving the discretized Poisson equation, the fast Fourier transform is used to ensure high accuracy as well as high efficiency.

B. Time-stepping algorithm

Here, the time-stepping algorithm to update the variables at the $(n + 1)$ -th time level from the n -th time level is briefly explained. Following the Simplified MAC method [1], corresponding to a standard incompressible fluid flow algorithm, with an incremental pressure correction applied to the finite difference scheme, we decompose the time-stepping into three steps.

In the first step, the second-order Adams-Bashforth scheme [5] is applied to explicitly updating the volume fraction $\phi_s^{(n+1)}$ and the modified left Cauchy-Green deformation tensor $\tilde{\mathbf{B}}^{(n+1)}$:

$$\phi_s^{(n+1)} = \phi_s^{(n)} - (\Delta t) \left(\frac{3}{2} \mathbf{v}^{(n)} \cdot \nabla \phi_s^{(n)} - \frac{1}{2} \mathbf{v}^{(n-1)} \cdot \nabla \phi_s^{(n-1)} \right), \quad (27)$$

$$\begin{aligned}
\tilde{\mathbf{B}}^{(n+1)} = & \tilde{\mathbf{B}}^{(n)} - (\Delta t) \left\{ \frac{3}{2} \mathbf{v}^{(n)} \cdot \nabla \tilde{\mathbf{B}}^{(n)} - \frac{1}{2} \mathbf{v}^{(n-1)} \cdot \nabla \tilde{\mathbf{B}}^{(n-1)} \right. \\
& + \frac{3}{2} \left(-\mathbf{L}^{(n)} \cdot \tilde{\mathbf{B}}^{(n)} - \tilde{\mathbf{B}}^{(n)} \cdot \mathbf{L}^{T(n)} \right) \\
& \left. - \frac{1}{2} \left(-\mathbf{L}^{(n-1)} \cdot \tilde{\mathbf{B}}^{(n-1)} - \tilde{\mathbf{B}}^{(n-1)} \cdot \mathbf{L}^{T(n-1)} \right) \right\},
\end{aligned} \tag{28}$$

where (Δt) denotes the time increment, and the superscript (n) stands for the n -th time level. It should be noted that (Δt) is chosen such that the Courant-Friedrichs-Lewy (CFL) condition is satisfied i.e. the CFL number based on the larger velocity scale between the maximum advection speed $\max(|v_x|, |v_y|)$ and the linear elastic wave speed $\sqrt{2(c_1 + c_2)/\rho}$ is 0.1 or less for all the present computations.

In the second step, the second-order Adams-Bashforth and Crank-Nicolson schemes [5] are applied to iteratively calculating the unprojected velocity vector \mathbf{v}^* and stress tensor $\tilde{\boldsymbol{\sigma}}^*$:

$$\begin{aligned}
\mathbf{v}^* = & \mathbf{v}^{(n)} - \frac{(\Delta t) \nabla \tilde{p}^{(n)}}{\rho} - (\Delta t) \left(\frac{3}{2} \mathbf{v}^{(n)} \cdot \nabla \mathbf{v}^{(n)} - \frac{1}{2} \mathbf{v}^{(n-1)} \cdot \nabla \mathbf{v}^{(n-1)} \right) \\
& + \frac{(\Delta t)}{\rho} \left(\frac{1}{2} \nabla \cdot \tilde{\boldsymbol{\sigma}}^* + \frac{1}{2} \nabla \cdot \tilde{\boldsymbol{\sigma}}^{(n)} \right),
\end{aligned} \tag{29}$$

$$\tilde{\boldsymbol{\sigma}}^* = (\mu_f + (\mu_s - \mu_f) \phi_s^{(n+1)}) (\nabla \mathbf{v}^* + \nabla \mathbf{v}^{*T}) + (\phi_s \tilde{\boldsymbol{\sigma}}_{sh})^{(n+1)}, \tag{30}$$

where the solid stress is given by (25).

Finally, pressure, solenoidal velocity vector, and stress tensor are updated during the projection step:

$$\tilde{p}^{(n+1)} = \tilde{p}^{(n)} + \varphi, \tag{31}$$

$$\mathbf{v}^{(n+1)} = \mathbf{v}^* - (\Delta t) \nabla \varphi, \tag{32}$$

$$\tilde{\boldsymbol{\sigma}}^{(n+1)} = \tilde{\boldsymbol{\sigma}}^* - 2(\Delta t) (\mu_f + (\mu_s - \mu_f) \phi_s^{(n+1)}) (\nabla \nabla \varphi), \tag{33}$$

where the incremental pressure φ is determined by solving the Poisson equation

$$\nabla^2 \varphi = \frac{\rho \nabla \cdot \mathbf{v}^*}{(\Delta t)}. \tag{34}$$

C. Spatial discretizations

The spatial derivatives are approximated by the second-order central differences, except for those of the advection terms in (13) and (22), to which the fifth-order WENO scheme [36, 45] is applied. For the momentum equation, following the spirit in [34, 38], we discretize the advection terms to satisfy the identity $\nabla \cdot (\mathbf{v} \mathbf{v}) = (\mathbf{v} \cdot \nabla) \mathbf{v} + \mathbf{v} (\nabla \cdot \mathbf{v})$ in the discretized space, that would make the energy highly conserved. The finite difference descriptions are detailed in Appendix A.

We here focus on the discretization of the right-hand-side of (22), that is important to accurately describe the isochoric solid deformation. We take care of the difference between the definition points of the diagonal \tilde{B}_{xx} , \tilde{B}_{yy} and non-diagonal \tilde{B}_{xy} components as illustrated in figure 4(b). The incompressibility $\det(\mathbf{B}) = 1$ implies $\tilde{B}_{xx} \tilde{B}_{yy} - \tilde{B}_{xy}^2 = \phi_s^{2\alpha}$. Since we choose $\alpha = 1/2$, we find

$$\frac{d}{dt} \iint_{\Omega} d^2 \mathbf{x} (\tilde{B}_{xx} \tilde{B}_{yy} - \tilde{B}_{xy}^2) = \frac{d}{dt} \iint_{\Omega} d^2 \mathbf{x} \phi_s = 0, \tag{35}$$

In consideration of the time derivative of each component of $\tilde{\mathbf{B}}$ in (22), the left-hand-side of (35) is given by

$$\begin{aligned}
& \iint_{\Omega} d^2 \mathbf{x} \left\{ (\partial_t \tilde{B}_{xx}) \tilde{B}_{yy} + \tilde{B}_{xx} (\partial_t \tilde{B}_{yy}) - 2(\partial_t \tilde{B}_{xy}) \tilde{B}_{xy} \right\} \\
= & \iint_{\Omega} d^2 \mathbf{x} \left\{ (-\mathbf{v} \cdot \nabla \tilde{B}_{xx}) \tilde{B}_{yy} + \tilde{B}_{xx} (-\mathbf{v} \cdot \nabla \tilde{B}_{yy}) - 2(-\mathbf{v} \cdot \nabla \tilde{B}_{xy}) \tilde{B}_{xy} \right\} \\
& + \iint_{\Omega} d^2 \mathbf{x} \left\{ \mathbf{e}_x \cdot (\mathbf{L} \cdot \tilde{\mathbf{B}} + \tilde{\mathbf{B}} \cdot \mathbf{L}^T) \cdot \mathbf{e}_x \tilde{B}_{yy} + \mathbf{e}_y \cdot (\mathbf{L} \cdot \tilde{\mathbf{B}} + \tilde{\mathbf{B}} \cdot \mathbf{L}^T) \cdot \mathbf{e}_y \tilde{B}_{xx} \right. \\
& \left. - 2\mathbf{e}_x \cdot (\mathbf{L} \cdot \tilde{\mathbf{B}} + \tilde{\mathbf{B}} \cdot \mathbf{L}^T) \cdot \mathbf{e}_y \tilde{B}_{xy} \right\},
\end{aligned} \tag{36}$$

where \mathbf{e} denotes the unit vector. Applying Gauss' divergence theorem together with the kinematic condition $\mathbf{n} \cdot \mathbf{v} = 0$ at the rigid wall Γ_w and the solenoidal condition (11), we rewrite the first term in the right-hand-side of (36) as

$$-\oint_{\Gamma_w} d\mathbf{x} \underbrace{\mathbf{n} \cdot \mathbf{v}}_{=0} \{ \tilde{B}_{xx} \tilde{B}_{yy} - \tilde{B}_{xy}^2 \} = 0.$$

Hence, in view of the solid volume conservation, the following relation should be satisfied:

$$\begin{aligned} \iint_{\Omega} d^2\mathbf{x} \{ \mathbf{e}_x \cdot (\mathbf{L} \cdot \tilde{\mathbf{B}} + \tilde{\mathbf{B}} \cdot \mathbf{L}^T) \cdot \mathbf{e}_x \tilde{B}_{yy} + \mathbf{e}_y \cdot (\mathbf{L} \cdot \tilde{\mathbf{B}} + \tilde{\mathbf{B}} \cdot \mathbf{L}^T) \cdot \mathbf{e}_y \tilde{B}_{xx} \\ - 2\mathbf{e}_x \cdot (\mathbf{L} \cdot \tilde{\mathbf{B}} + \tilde{\mathbf{B}} \cdot \mathbf{L}^T) \cdot \mathbf{e}_y \tilde{B}_{xy} \} = 0. \end{aligned} \quad (37)$$

We choose the interpolation and the finite difference formulae to satisfy the integral relation (37) in a discrete form. For a quantity q , let us introduce finite difference operators δ_i and δ_j , of which the indices i and j correspond to discretized coordinates along the respective directions x and y , such as

$$\delta_i(q)|_{i,j} = q_{i+\frac{1}{2},j} - q_{i-\frac{1}{2},j}, \quad \delta_j(q)|_{i,j} = q_{i,j+\frac{1}{2}} - q_{i,j-\frac{1}{2}}, \quad (38)$$

and a four-point interpolation operator denoted by double overline such as

$$\overline{\overline{q}}|_{i,j} = \frac{q_{i-\frac{1}{2},j-\frac{1}{2}} + q_{i+\frac{1}{2},j-\frac{1}{2}} + q_{i-\frac{1}{2},j+\frac{1}{2}} + q_{i+\frac{1}{2},j+\frac{1}{2}}}{4}. \quad (39)$$

The integral $\int_{\Omega} d^2\mathbf{x} f g$ provides the equality in a finite volume representation

$$\sum_i \sum_j \Delta_x \Delta_y f_{i,j} \overline{\overline{g}}|_{i,j} = \sum_i \sum_j \Delta_x \Delta_y \overline{\overline{f}}|_{i+\frac{1}{2},j+\frac{1}{2}} g_{i+\frac{1}{2},j+\frac{1}{2}}, \quad (40)$$

where the quantities f and g are defined at the cell center and at the cell apex, respectively, and assumed to vanish at the boundary Γ_W . We write each component of $\mathbf{L} \cdot \tilde{\mathbf{B}} + \tilde{\mathbf{B}} \cdot \mathbf{L}^T$ involved in (37) as

$$\left(\mathbf{e}_x \cdot (\mathbf{L} \cdot \tilde{\mathbf{B}} + \tilde{\mathbf{B}} \cdot \mathbf{L}^T) \cdot \mathbf{e}_x \right)_{i,j} = 2L_{xx,i,j} \tilde{B}_{xx,i,j} + 2\overline{\overline{L_{xy} \tilde{B}_{xy}}}|_{i,j}, \quad (41)$$

$$\left(\mathbf{e}_y \cdot (\mathbf{L} \cdot \tilde{\mathbf{B}} + \tilde{\mathbf{B}} \cdot \mathbf{L}^T) \cdot \mathbf{e}_y \right)_{i,j} = 2L_{yy,i,j} \tilde{B}_{yy,i,j} + 2\overline{\overline{L_{yx} \tilde{B}_{xy}}}|_{i,j}, \quad (42)$$

$$\begin{aligned} \left(\mathbf{e}_x \cdot (\mathbf{L} \cdot \tilde{\mathbf{B}} + \tilde{\mathbf{B}} \cdot \mathbf{L}^T) \cdot \mathbf{e}_y \right)_{i+\frac{1}{2},j+\frac{1}{2}} &= \left(\overline{\overline{L_{xx}}}|_{i+\frac{1}{2},j+\frac{1}{2}} + \overline{\overline{L_{yy}}}|_{i+\frac{1}{2},j+\frac{1}{2}} \right) \tilde{B}_{xy,i+\frac{1}{2},j+\frac{1}{2}} \\ &+ L_{xy,i+\frac{1}{2},j+\frac{1}{2}} \overline{\overline{\tilde{B}_{yy}}}|_{i+\frac{1}{2},j+\frac{1}{2}} + L_{yx,i+\frac{1}{2},j+\frac{1}{2}} \overline{\overline{\tilde{B}_{xx}}}|_{i+\frac{1}{2},j+\frac{1}{2}}, \end{aligned} \quad (43)$$

where

$$L_{xx,i,j} = \frac{\delta_i(v_x)|_{i,j}}{\Delta_x}, \quad L_{yy,i,j} = \frac{\delta_j(v_y)|_{i,j}}{\Delta_y},$$

$$L_{xy,i+\frac{1}{2},j+\frac{1}{2}} = \frac{\delta_j(v_x)|_{i+\frac{1}{2},j+\frac{1}{2}}}{\Delta_y}, \quad L_{yx,i+\frac{1}{2},j+\frac{1}{2}} = \frac{\delta_i(v_y)|_{i+\frac{1}{2},j+\frac{1}{2}}}{\Delta_x}.$$

Substituting (41)–(43) into (37) together with the relation (40), and considering the solenoidal condition (11), we confirm that the requirement (37) would be fulfilled in a discrete form as

$$2 \sum_i \sum_j \Delta_x \Delta_y \underbrace{(L_{xx,i,j} + L_{yy,i,j})}_{=0} \left(\tilde{B}_{xx,i,j} \tilde{B}_{yy,i,j} - \overline{\overline{\tilde{B}_{xy}^2}}|_{i,j} \right) = 0.$$

IV. VALIDATION TESTS

For the purpose of addressing several computational issues involved in the procedure advocated in §II and §III, firstly, we consider a one-dimensional problem for the motion of the oscillatory parallel fluid-solid layers. Though this system is a simple example, it includes the fundamental aspects of the FSI problem and the system allows estimate of the numerical accuracy in the present full Eulerian approach as it has analytical solutions. In the second example for validation, we make comparisons with the available data of the deformable solid motion in a lid-driven cavity [97] and the particle-particle interaction in a Couette flow [12]. Also, in the third example, a response of hyperelastic material to the external shear strain is examined to check the reversibility in shape as this aspect is vital for a full Eulerian formulation.

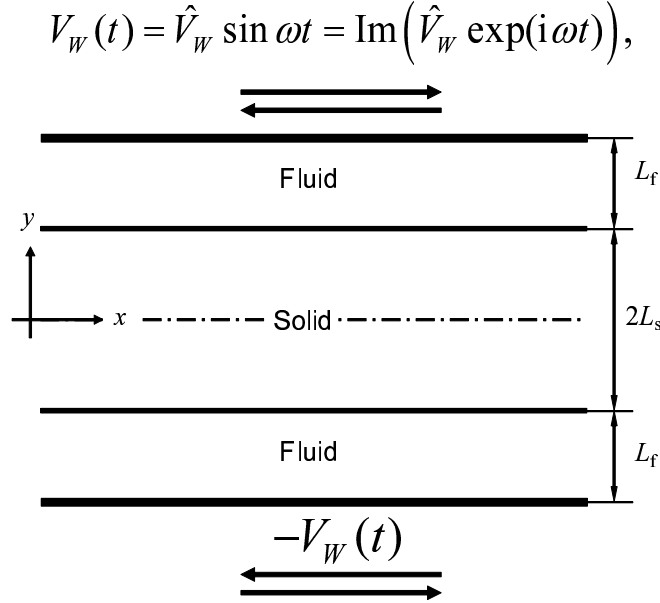


FIG. 5: Schematic figure of the parallel fluid-structure layers. The upper and lower plates move in opposite directions with temporally sinusoidal velocities to drive the fluid and solid motions.

A. Oscillatory response in parallel layers of fluid and solid

As schematically illustrated in figure 5, we deal with the interactive motions of the three (fluid-solid-fluid) parallel layers bounded with two oscillatory plane walls. Here, making comparisons with accurate solutions obtained by means of a sharp interface approach, we examine the validation and verification of the present Eulerian approach, accompanied with a diffuse interface. Supposing homogeneity in x direction, we may omit the x -dependence of any quantity in the theoretical analysis. In the numerical simulation, the periodic condition is applied in x direction. We here treat pure hyperelastic material, i.e., $\mu_s = 0$. The relations between the velocity v , the displacement u and the shear stress σ are given by

$$\partial_t v = \partial_y \sigma, \quad (44)$$

$$\partial_t u = v, \quad (45)$$

$$\sigma = \begin{cases} \mu_f \partial_y v & \text{for fluid } (L_s < |y| \leq L_s + L_f), \\ 2(c_1 + c_2) \partial_y u + 4c_3 (\partial_y u)^3 & \text{for solid } (0 \leq |y| < L_s), \end{cases} \quad (46)$$

with no-slip condition at the upper and lower plates ($y = \pm(L_f + L_s)$)

$$v = \begin{cases} \hat{V}_W \sin \omega t & \text{at } y = L_f + L_s, \\ -\hat{V}_W \sin \omega t & \text{at } y = -(L_f + L_s). \end{cases} \quad (47)$$

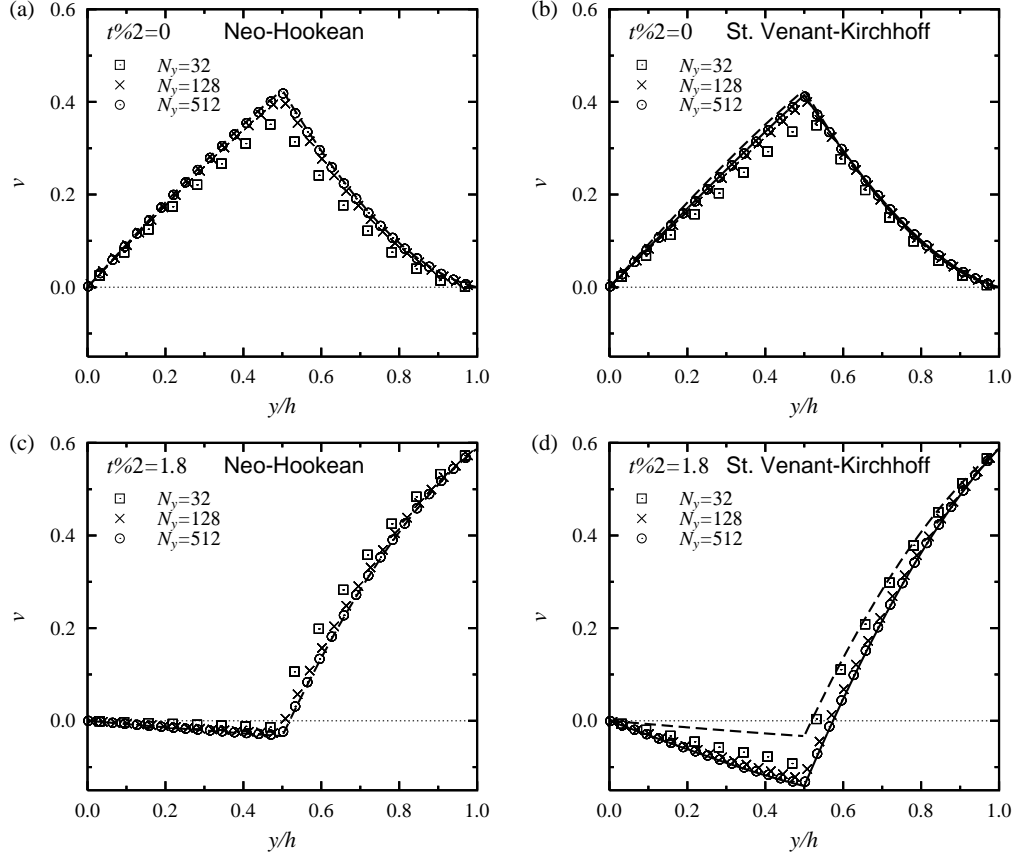


FIG. 6: The velocity profile in the upper half region of the parallel fluid-structure layers under the conditions of $\mu_f = 1$, $L_s = L_f = 0.5$, $\omega = \pi$, and $\hat{V}_w = 1$. Left panels: the neo-Hookean material with the modulus of transverse elasticity of $G = 5$. Right panels: the incompressible Saint Venant-Kirchhoff material with the Lamé constants of $\lambda_{\text{Lamé}}^s = 7.5$ and $\mu_{\text{Lamé}}^s = 5$. The upper and lower panels show the results at the temporal phases of $t\%2 = 0$ and $t\%2 = 1.8$, respectively. The dashed and solid curves respectively represent the linear and nonlinear solutions with the sharp interface, which are determined by means of the spectral approach (see Appendix B). The symbols correspond to the present Eulerian simulation results for various number of grid points ($N_x \times N_y = 8 \times 32, 8 \times 128, 8 \times 512$).

The solid stress expression (46) indicates that the system involving a linear Mooney-Rivlin material with $c_3 = 0$ is linear with respect to the displacement u , while that involving the Saint Venant-Kirchhoff material with $c_3 \neq 0$ is nonlinear.

The simulation results based on the present full Eulerian approach are compared with the analytical solution obtained by means of the sharp interface approach (see Appendix B for detail). We fix the conditions $\rho = 1$, $\mu_f = 1$, $L_x = 8$, $L_s = L_f = 0.5$, $\omega = \pi$, and $\hat{V}_w = 1$, and vary the number of grid points ($N_x \times N_y = 8 \times 32, 8 \times 128, 8 \times 512$). Initially, the system is at rest. The total computational period is $t = 40$, corresponding to 20 cycles, and the sampling is performed within the last one cycle i.e., $t \in (38, 40]$. Figure 6 shows the velocity profiles for the neo-Hookean model ($G = 5$, i.e., $c_1 = 2.5$, $c_2 = c_3 = 0$) and for the Saint Venant-Kirchhoff one ($\lambda_{\text{Lamé}}^s = 7.5$, $\mu_{\text{Lamé}}^s = 5$, i.e., $c_1 = 5.0$, $c_2 = -2.5$, $c_3 = 2.1875$). The present simulation results converge to the sharp interface solutions with the higher spatial resolution. Figure 6(d) shows the obvious difference in profile between the linear ($c_3 = 0$) and nonlinear ($c_3 \neq 0$) solutions at the phase of $t\%2 = 1.8$ (here % stands for the remainder). The simulation results in figure 6(d) clearly get closer to the nonlinear solution with increasing the number of grid points, indicating that the nonlinearity in the solid constitutive law is reasonably captured in the present Eulerian approach.

The accuracy in the fluid-structure coupling is quantified by the errors in L_2 and L_∞ norms, which are respectively

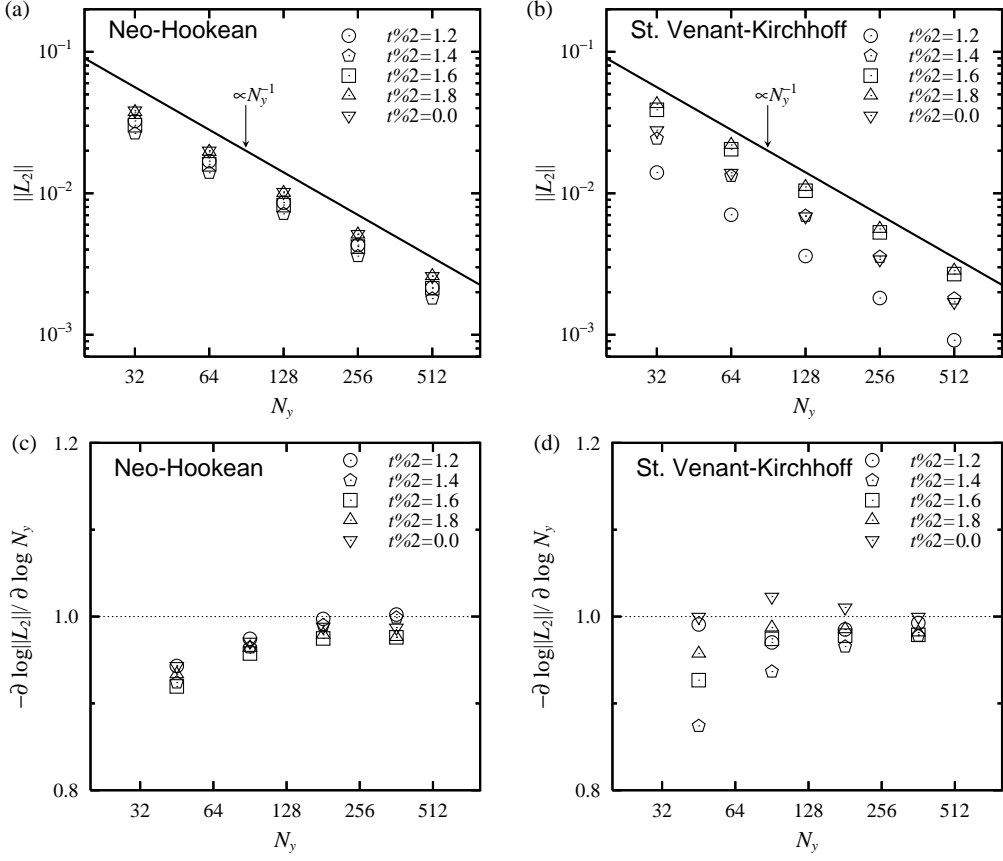


FIG. 7: Upper panels: The error of the velocity in L_2 norm versus the number N_y of grid points in the vertical (y) direction for various temporal phases in the parallel fluid-structure layers. The error is determined from the difference between the results of the present Eulerian and sharp interface methods based on (48). Lower panels: The absolute slope in the plot of the error versus N_y . The local slope is determined from (49). The left and right panels correspond to the neo-Hookean and incompressible Saint-Venant Kirchhoff materials, respectively. The conditions are the same as those of figure 6.

defined as

$$\begin{aligned} \|L_2\|(N_y) &= \left\{ \frac{1}{N_y} \sum_{j=1}^{N_y} (v_j^{(n)} - v_j^{(a)})^2 \right\}^{\frac{1}{2}}, \\ \|L_\infty\|(N_y) &= \max_{j \in [1, N_y]} |v_j^{(n)} - v_j^{(a)}|, \end{aligned} \quad (48)$$

where $v_j^{(n)}$ and $v_j^{(a)}$, respectively, denote the present result and the sharp interface solution on the node $y_j = (j - \frac{1}{2})/N_y$. The log-log plots of the L_2 and L_∞ errors versus the number of grid points are shown in figure 7(a)(b) and figure 8(a)(b), respectively. The local slopes are obtained therefrom, and shown in figure 7(c)(d) and figure 8(c)(d). Here, the local slopes are determined from the following approximations

$$\begin{aligned} \frac{\partial \log(\|L_2\|)}{\partial \log(N_y)}(N_y) &\approx \frac{\log(\|L_2\|(\sqrt{2}N_y)) - \log(\|L_2\|(N_y/\sqrt{2}))}{\log 2}, \\ \frac{\partial \log(\|L_\infty\|)}{\partial \log(N_y)}(N_y) &\approx \frac{\log(\|L_\infty\|(\sqrt{2}N_y)) - \log(\|L_\infty\|(N_y/\sqrt{2}))}{\log 2}. \end{aligned} \quad (49)$$

The slope indicates the degree of the accuracy in the fluid-structure coupling. In both the L_2 error (corresponding to a global indicator) and the L_∞ error (corresponding to a local maximum indicator) are nearly proportional to N_y^{-1} . Since the second-order finite difference is applied to describing the spatial derivatives, this near-first order trend must

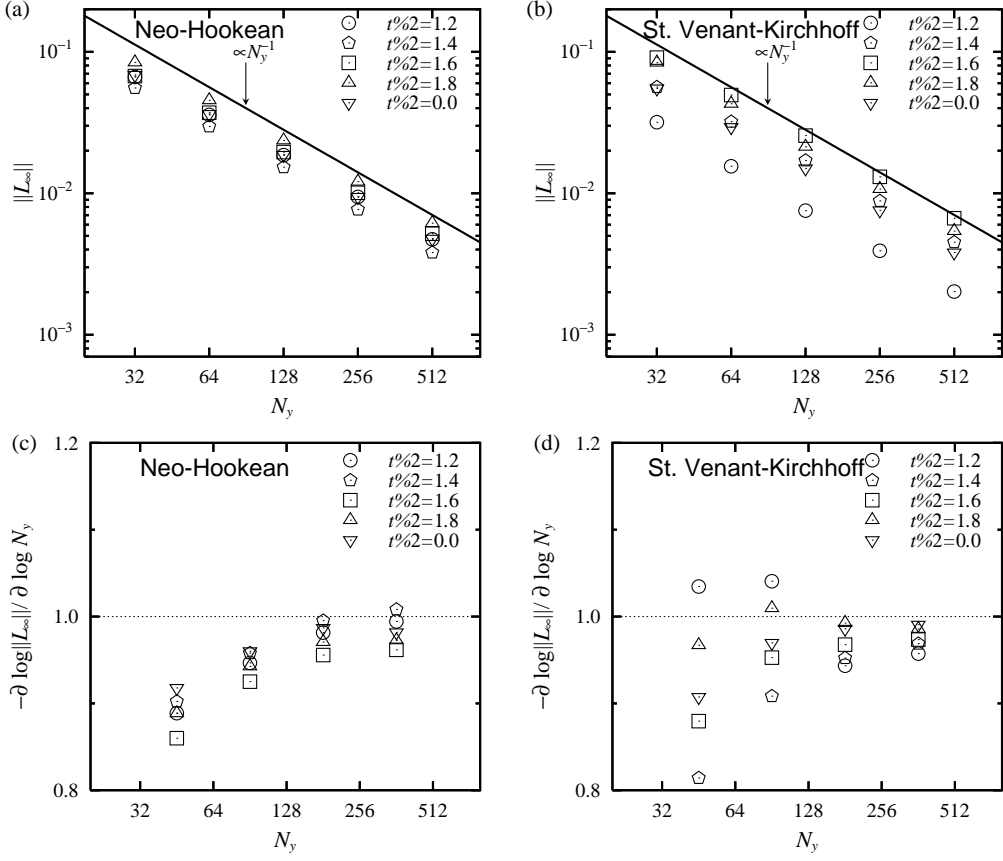


FIG. 8: Same as figure 7, but in L_∞ norm.

have resulted from the mixture stress expression (9) involving the first-order accuracy locally at the interface, which dominates the global degree of accuracy. Note that we also investigated the grid convergence of the shear stress, and confirmed that the accuracy at the interface is of the first-order with respect to the grid size.

Figure 9 shows the sensitivity of the wall friction amplitude $\tau_{w,\text{rms}}$ on moduli. We fix the conditions $\mu_f = 1$, $\mu_s = 0$, $L_s = L_f = 0.5$, $\omega = \pi$, and $\hat{V}_w = 1$. Likewise the computations in figure 6, the total computational period is set to 20 cycles. The root-mean-square of τ_w was sampled over the last one cycle. The results of the linear Mooney-Rivlin model with ($c_2 = c_1/2$, $c_3 = 0$) as well as the neo-Hookean ($c_2 = c_3 = 0$) and Saint Venant-Kirchhoff ($c_2 = -c_1/2$, $c_3 = 7c_1/16$) models are plotted as a function of $2(c_1 + c_2)$. Because the deformed motion of solid behaves like as the spring-mass system, the plot of the wall friction amplitude versus $2(c_1 + c_2)$ reveals the non-monotonous resonant behavior. As long as the solid strain is sufficiently small, the nonlinearity involved in the constitutive law is negligible, and therefore the linear assumption is justified. Indeed, the curve of the nonlinear solution approaches the linear solution with increasing $2(c_1 + c_2)$ since the solid strain is suppressed for the stiffer material. By contrast, for the smaller $2(c_1 + c_2)$, the discrepancy between the linear and nonlinear solutions becomes more obvious. It is because the larger strain makes the nonlinear system effectively stiffer as implied by (46). All the results of the present Eulerian approach are in good agreement with the sharp interface solution. The present approach is confirmed to capture the resonance behavior resulting from the dynamic interaction between the fluid and solid motions, and the nonlinearity in the solid constitutive law.

B. Comparison with independently conducted FSI analyses

We here make comparisons with two well-validated FSI analyses. In the constitutive law for (visco-)hyperelastic material, one has $\mu_s = \mu_f$, $c_1 \neq 0$ and $c_2 = c_3 = 0$, and the other has $\mu_s = 0$, $c_2 \neq 0$ and $c_1 = c_3 = 0$.

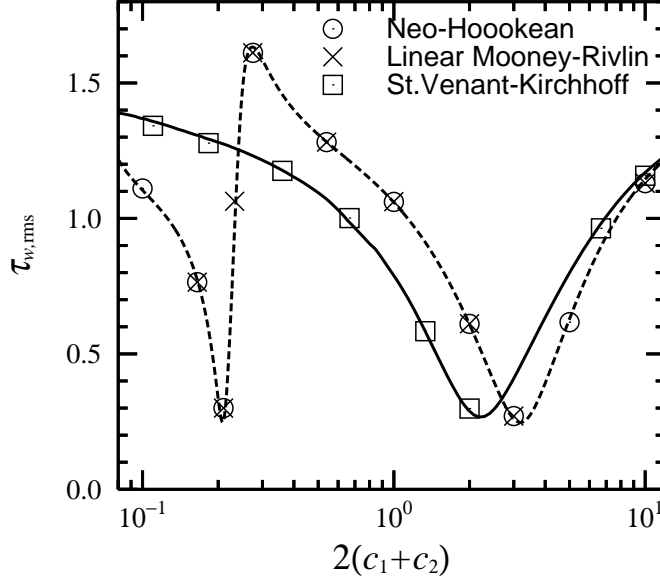


FIG. 9: Response curve of the skin friction amplitude $\tau_{w,rms}$ in the motion of the parallel fluid-structure layers as a function of $2(c_1 + c_2)$ with $\mu_f = 1$, $L_s = L_f = 0.5$, $\omega = \pi$, and $\hat{V}_w = 1$. The symbols correspond to the results based on the present Eulerian method with the 8×256 mesh. The circles, crosses, and squares represent results of the neo-Hookean ($c_2 = c_3 = 0$), linear Mooney-Rivlin ($c_2 = c_1/2$, $c_3 = 0$) and incompressible Saint Venant-Kirchhoff ($c_2 = -c_1/2$, $c_3 = 7c_1/16$) models, respectively. The curves represent the sharp interface solutions, which are determined by means of the spectral methods (see Appendix B). The dashed curve represents the linear solution for the neo-Hookean and linear Mooney-Rivlin materials with $c_3 = 0$, while the solid curve the nonlinear solution for the above-mentioned Saint Venant-Kirchhoff material.

1. A solid motion in a lid-driven cavity flow

We perform full Eulerian simulations of deformable solid motion in a lid-driven cavity with the same setup and conditions as Zhao *et al.* [97], who employed mixed Lagrangian and Eulerian approach. The initial setup is schematically illustrated in figure 10(a). The size of the cavity is $L_x \times L_y = 1 \times 1$. Initially, the system is at rest. The unstressed solid shape is circular with a radius of 0.2, and centered at (0.6, 0.5). At $t = 0$, to drive the fluid and solid motions, the top wall starts to move at a speed of $V_W = 1$ in x direction. The no-slip condition is imposed on the walls. The solid component is neo-Hookean material. The material properties are $\rho = 1$, $\mu_f = \mu_s = 10^{-2}$, $c_1 = 0.05$ and $c_2 = c_3 = 0$.

Figure 10 visualizes the particle deformation and the flow field for eight consecutive time instants. The dashed curve in figure 10 represents the outline of the particle obtained by Zhao *et al.* [97], in which they computed the solid deformation on the Lagrangian mesh. The solid lines represent the instantaneous particle shapes, corresponding to the isoline at $\phi_s = 1/2$, obtained by the present full Eulerian simulation. The dotted material points are tracked just to transfer images of the particle deformation, but we did not use these material points for computing solid stress and strain. The particle moves and deforms driven by the fluid flow, and exhibits highly deformed shape when the particle approaches the wall. It should be noticed that no special artifact for avoiding a particle-wall overlap is implemented into the present method because the particle-wall hydrodynamic repulsion is likely to be brought by the soft lubrication effect [67] due to the geometry change via the particle deformation. The solid shapes obtained by the present Eulerian simulation are in excellent agreement with the well-validated result [97].

In addition to the comparative study, we address grid convergence issues below. We trace the centroid $\mathbf{x}_c = (x_c, y_c)$ of the particle, which is evaluated from the approximation

$$\mathbf{x}_c(t) \approx \frac{\sum_{i=1}^{N_x} \sum_{j=1}^{N_y} \Delta x \Delta y \mathbf{x}_{i,j} \phi_s(\mathbf{x}_{i,j}, t)}{\sum_{i=1}^{N_x} \sum_{j=1}^{N_y} \Delta x \Delta y \phi_s(\mathbf{x}_{i,j}, t)}. \quad (50)$$

Figure 11 shows the trajectory of the centroid \mathbf{x}_c in a time range of $t \in [0, 20]$ for various number of grid points

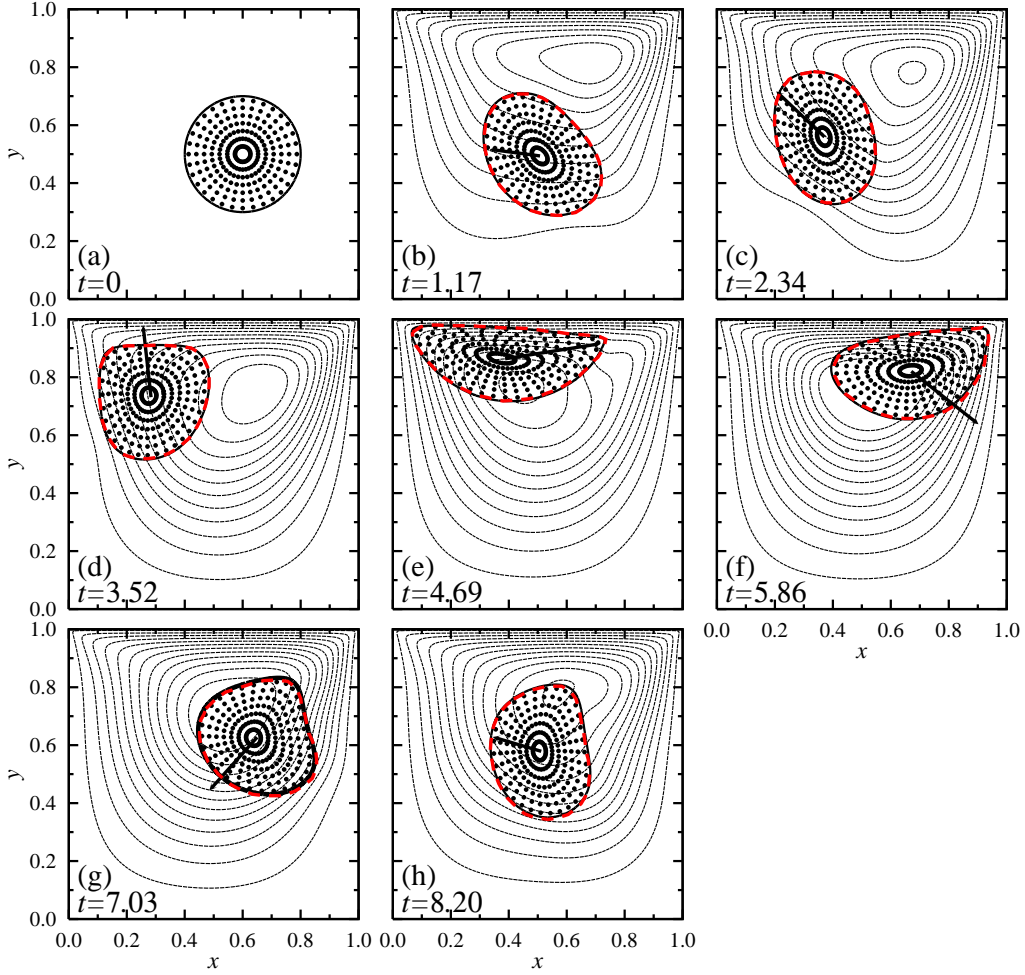


FIG. 10: Comparison of the solid deformation in the lid-driven flow with the simulation result [97]. The dashed outline represents the result of Zhao *et al.* [97], in which the Lagrangian tracking approach was employed to describe the solid deformation. The solid outline, the dotted material points and the streamlines correspond to the present simulation results based on the full Eulerian approach with a mesh 1024×1024 .

($N_x \times N_y = 64 \times 64, 128 \times 128, 256 \times 256, 512 \times 512, 1024 \times 1024$). The trajectories clearly exhibit a convergent trend to the curve of the highest spatial resolution.

To quantify the grid convergence behavior, the distance of the particle centroid \mathbf{x}_c with respect to that of the highest resolution $N_x = 1024$ is monitored. We evaluate the errors in L_2 and L_∞ norms respectively from

$$\begin{aligned} ||L_2|| (N_x) &= \left\{ \frac{1}{T} \int_0^T dt |\mathbf{x}_c(t, N_x) - \mathbf{x}_c(t, N_x = 1024)|^2 \right\}^{\frac{1}{2}}, \\ ||L_\infty|| (N_x) &= \max_{t \in [0, T]} |\mathbf{x}_c(t, N_x) - \mathbf{x}_c(t, N_x = 1024)|. \end{aligned} \quad (51)$$

Figure 12 shows the L_2 and L_∞ errors as a function of N_x . Both the errors are nearly proportional to N_x^{-1} , indicating the first-order accuracy. The first-order accuracy involved in the fluid-structure coupling as described in §IV A is reflected on the slopes in these plots.

In addition to the particle centroid, to further examine the grid convergence behavior, we here perform modal analyses of the particle deformation. The distance from the particle centroid \mathbf{x}_c to the interface $\mathbf{x}_I = (x_I, y_I)$ is written as

$$R(\theta) = |\mathbf{x}_I - \mathbf{x}_c|, \quad (52)$$

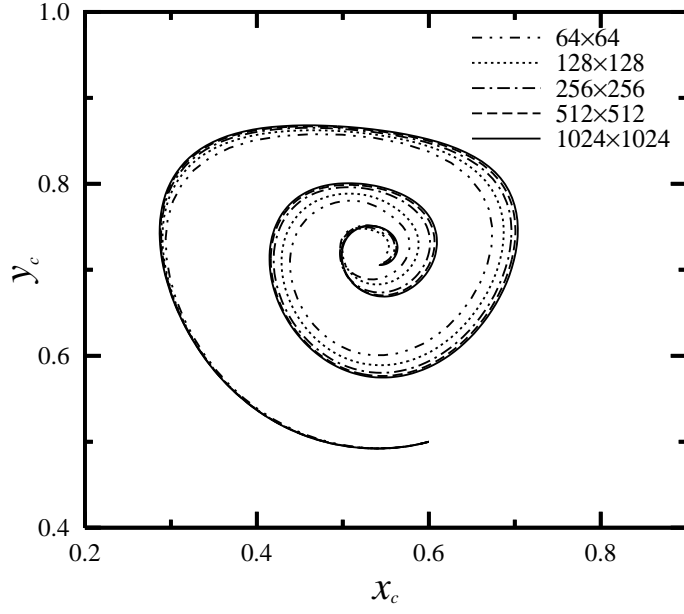


FIG. 11: Trajectories of the solid centroid in the lid-driven flow in a time range $t \in [0, 20]$ for various number of grid points.

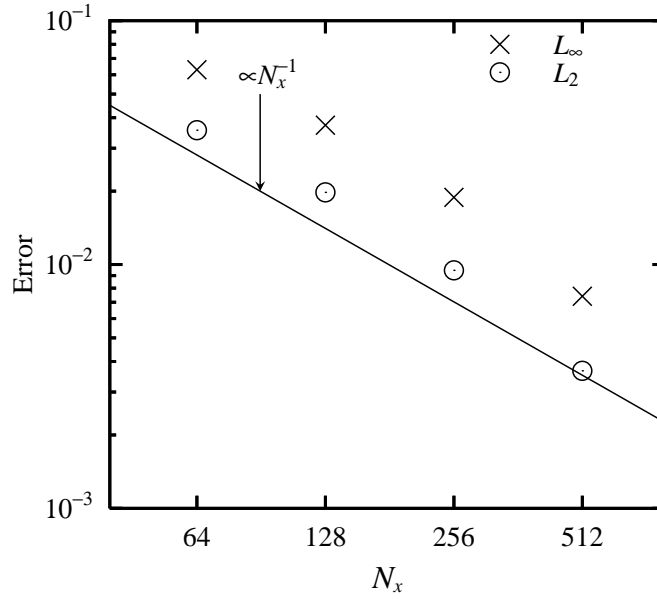


FIG. 12: The errors of the particle centroid in L_2 norm and in L_∞ norm versus the number N_x of grid points in the lid-driven flow.

where θ is found to satisfy the relations

$$\cos \theta = \frac{x_I - x_c}{|\mathbf{x}_I - \mathbf{x}_c|}, \quad \sin \theta = \frac{y_I - y_c}{|\mathbf{x}_I - \mathbf{x}_c|}. \quad (53)$$

The distance is written in a Fourier series form

$$R(\theta) = R_0 + \sum_{n=1}^{\infty} (R_{cn} \cos n\theta + R_{sn} \sin n\theta), \quad (54)$$

where R_n denotes the n -th order deformation mode. The deformation modes are uniquely determined via the orthog-

onality in the cosine and sine functions from definite integrals

$$\begin{aligned} R_0 &= \frac{1}{2\pi} \int_0^{2\pi} d\theta R(\theta), \\ R_{cn} &= \frac{1}{\pi} \int_0^{2\pi} d\theta R(\theta) \cos n\theta, \quad R_{sn} = \frac{1}{\pi} \int_0^{2\pi} d\theta R(\theta) \sin n\theta. \end{aligned} \quad (55)$$

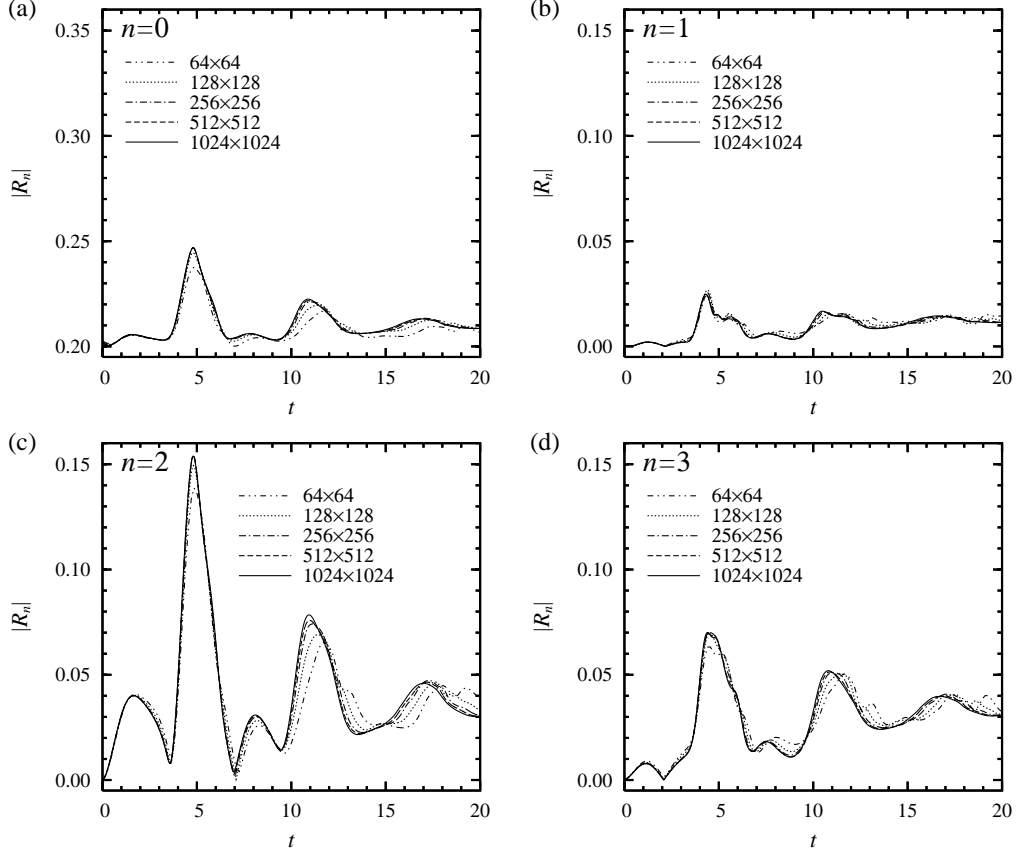


FIG. 13: Time history of the n -th order modal amplitude $|R_n|$ of the particle deformation in the lid-driven cavity flow for various number of grid points. (a) $n = 0$, (b) $n = 1$, (c) $n = 2$, and (d) $n = 3$.

In the present Eulerian approach, the fluid and solid phases are distinguished by the solid volume fraction ϕ_s , and there is no explicit quantity describing the angular profile of R . Instead of the circumferential integral in (55), we will apply the area integral to evaluating the deformation mode. Let us consider the following relation for a function $f(\theta)$:

$$\int_0^{2\pi} d\theta R(\theta) f(\theta) = \iint_{\Omega} d^2\mathbf{x} \delta(|\mathbf{x} - \mathbf{x}_I|) f(\theta), \quad (56)$$

where δ stands for a one-dimensional Dirac's delta function, which is related to the gradient of the solid indicator function I_s , namely,

$$\nabla I_s = -\mathbf{n} \delta(|\mathbf{x} - \mathbf{x}_I|),$$

where \mathbf{n} denotes the unit normal vector pointing towards the fluid and is given by

$$\mathbf{n} = -\frac{\nabla I_s}{|\nabla I_s|}.$$

Hence, the delta function used in (56) is expressed as

$$\delta(|\mathbf{x} - \mathbf{x}_I|) = |\nabla I_s|.$$

Implementing (56) in the finite difference approach, one must smooth the delta function at the grid scale. Upon using the solid volume fraction ϕ_s , which is regarded as the solid indicator function smoothed at the grid scale, we obtain the approximation

$$\delta(|\mathbf{x} - \mathbf{x}_I|) \approx |\nabla \phi_s|, \quad (57)$$

and then evaluate the definite integrals in the summation form

$$\int_0^{2\pi} d\theta R(\theta) f(\theta) \approx \sum_{i=1}^{N_x} \sum_{j=1}^{N_y} \Delta_x \Delta_y |\nabla \phi_{s,i,j}| f(\theta_{i,j}), \quad (58)$$

together with (50) to find $\theta_{i,j} = \theta(\mathbf{x}_{I,i,j}, \mathbf{x}_c)$. For $n \geq 1$, we write the modal amplitude as $|R_n| = \sqrt{R_{cn}^2 + R_{sn}^2}$.

Figure 13 shows the temporal evolutions of the modal amplitude $|R_n|$ ($n = 0, 1, 2$ and 3) of the particle deformation for various number of grid points. The largest elongation ($n = 2$ mode) of the particle is observed at about $t = 5$ when the particle is in the proximity of the moving wall, and the synchronized increases in $|R_n|$ are found for different modes. With increasing the number of grid points, the profiles for each mode n settle to corresponding convergent curves, suggesting the verification with respect to the deformation of the particles.

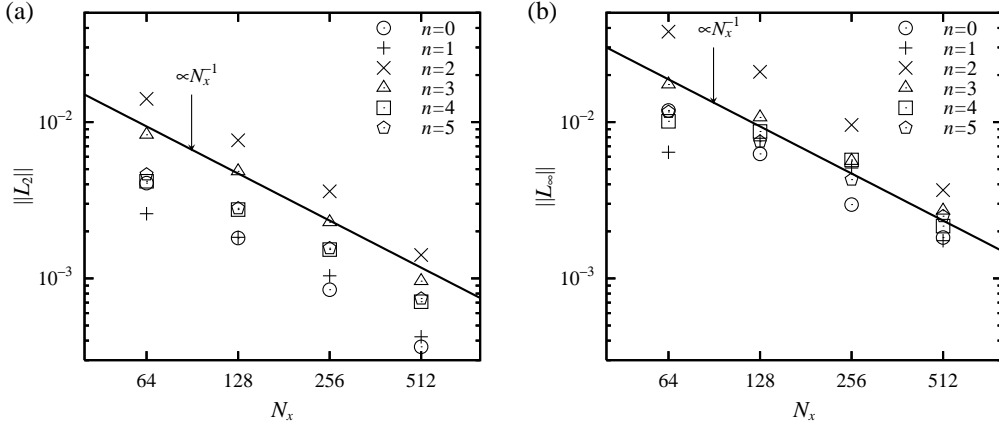


FIG. 14: The errors of the n -th order modal amplitude $|R_n|$ ($n = 0, 1, 2, 3, 4$ and 5) of the particle deformation (a) in L_2 norm and (b) in L_∞ norm versus the number N_x of grid points in the lid-driven flow.

In a similar manner to (51), the L_2 and L_∞ errors of the modal amplitude with respect to that of the highest resolution $N_x = 1024$ are quantified as follows:

$$\begin{aligned} ||L_2|| (N_x) &= \left\{ \frac{1}{T} \int_0^T dt \left| |R_n|(t, N_x) - |R_n|(t, N_x = 1024) \right|^2 \right\}^{\frac{1}{2}}, \\ ||L_\infty|| (N_x) &= \max_{t \in [0, T]} \left| |R_n|(t, N_x) - |R_n|(t, N_x = 1024) \right|. \end{aligned} \quad (59)$$

Figure 14 shows the L_2 and L_∞ errors as a function of N_x . Again, both the errors are nearly proportional to N_x^{-1} , indicating the first-order accuracy for capturing the particle deformation.

2. Two particles interaction in a Couette flow

We here make a comparison with the available numerical analysis of the interaction between two deformable particles in a Couette flow performed by Gao & Hu [12], who adopted body-fit Lagrangian mesh. The computational extent is $L_x \times L_y = 8 \times 4$, which is the same as [12]. Initially, the system is at rest. Two unstressed solid particles are

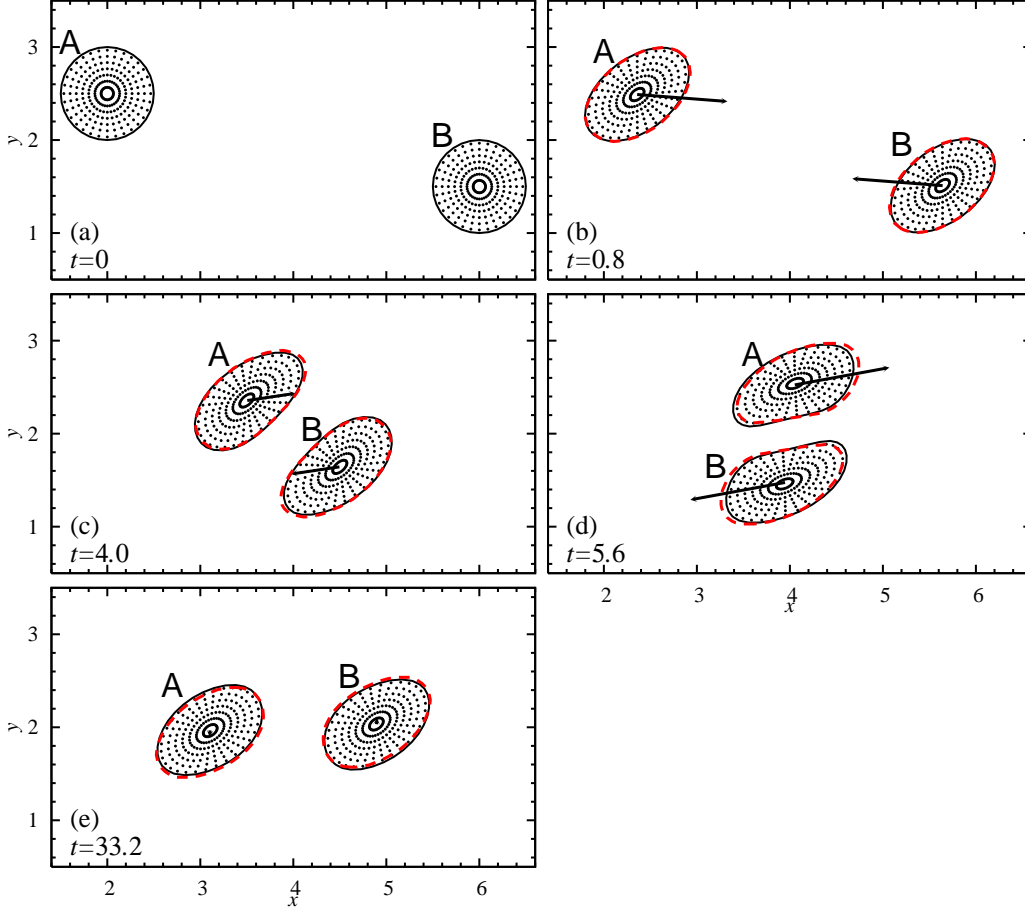


FIG. 15: Comparison of particle-particle interactions in a Couette flow with the simulation result [12]. The dashed outline represents the result of Gao & Hu [12], in which the body-fit Lagrangian mesh was used to solve the FSI problem. The dotted material points and the solid outline correspond to the present simulation results based on the full Eulerian approach with a mesh 1024×512 . At $t = 0.8$, initial deformation; At $t = 4.0$ and $t = 5.6$, “roll over” interacting mode; At $t = 33.2$, “bounce back” interacting mode [12].

initially circular with a radius of 0.5, and centered at $\mathbf{x}_{c,A} = (2, 2.5)$ and $\mathbf{x}_{c,B} = (6, 1.5)$ as depicted in figure 15(a). The upper and lower plates located at $y = 4$ and $y = 0$, respectively, start to move impulsively to drive the fluid and solid motions at speeds of $V_W^{\text{upper}} = 1$ and $V_W^{\text{lower}} = -1$ in x direction.

The no-slip condition is imposed on the plates, while the periodic condition is applied in x direction. The solid component is purely hyperelastic. The material properties are $\rho = 1$, $\mu_f = 20$, $\mu_s = 0$, $c_2 = 40$ and $c_1 = c_3 = 0$.

Figure 15 visualizes the two-particle shape for five time instants. The dotted markers are, again, to represent the solid deformations and those markers are not used for computing solid stress or strain. The arrows at the particle centers are the instantaneous translating velocity vectors. The dashed curve in figure 15 represents the outline of the particles obtained by Gao & Hu [12]. The particles experience somehow complicated interactions involving the “roll over” and “bounce back” modes as examined in [12]. The solid shape obtained by the present Eulerian simulation is again in agreement with the well-validated result [12], indicating that the particle-particle interaction is also reasonably captured by the present approach.

Figure 16 shows the temporal evolution of the y_c -position of the particle centroid, which is evaluated from (50), for various grid resolutions ($N_x \times N_y = 128 \times 64, 256 \times 128, 512 \times 256, 1024 \times 512$). In the full Lagrangian computation [12], the finite element mesh is refined within the particle-particle gap, whereas in the present Eulerian simulation, the grid size is uniform and fixed. When the plot shows peaks around $t = 3.0$, $t = 16.0$ and $t = 20.0$, the gap between the particles is narrow, and the particle undergoes relatively strong hydrodynamic force owing to a squeezing effect. Such a narrow-gap effect is less resolved by the present method than the full Lagrangian method especially for the low spatial resolution cases, that is reflected on the larger deviations from the result by Gao & Hu [12] preferentially

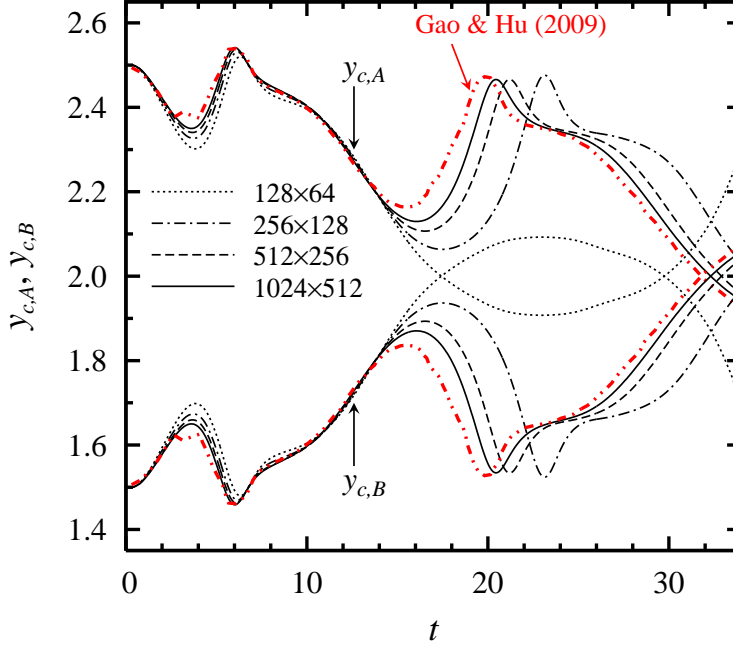


FIG. 16: Variations of particle y_c -position as functions of time for various number of grid points. Comparison with the result of Gao & Hu[12].

at the peaks. In the higher spatial resolution, the profiles of the present simulation get closer to the full Lagrangian result [12].

C. Reversibility in shape of hyperelastic material

The hyperelastic material generally exhibits reversibility in shape when it is released from stress. In the total Lagrangian method using the finite element mesh, since the tracked material point links both the reference and current configurations, the reversibility can be captured with little difficulty. By contrast, the Eulerian fixed grid point retains no information on the reference configuration. Therefore, one may raise a shortcoming that the Eulerian approach is likely to lose the information about the original shape once the material is stressed to deform. We here perform a reversibility examination.

1. For a circular particle

We here deal with a shear flow between two plane plates involving a hyperelastic particle. The distance between the plates is $L_y = 2$. The computational extent in x direction is set to $L_x = 8$. The upper and lower plates are located at $y = 1$ and $y = -1$, respectively. Initially, the system is at rest. An unstressed solid particle is initially circular with a radius of 0.75, and centered at the middle position $(0, 0)$ between the plates as depicted in figure 17(a). The no-slip condition is imposed on the plates, whereas the periodic condition is applied in x direction. We fix the material properties $\rho = 1$, $\mu_f = 1$ and $\mu_s = 0$. We consider two kinds of materials: one is the linear Mooney-Rivlin material with $c_1 = 4$, $c_2 = 2$ and $c_3 = 0$, and the other is the Saint Venant-Kirchhoff material with $\lambda_{\text{Lamé}}^s = 6$ and $\mu_{\text{Lamé}}^s = 4$ (i.e., $c_1 = 4$, $c_2 = -2$ and $c_3 = 1.75$).

The system motion is controlled as follows. Within a period of $0 \leq t \leq 4$, the upper and lower plates move at speeds of $V_W^{\text{upper}} = 1$ and $V_W^{\text{lower}} = -1$ in x direction, respectively, to drive the fluid and solid motions. After $t = 4$, the moving plates stop (i.e. $V_W^{\text{upper}} = V_W^{\text{lower}} = 0$) to release the particle from the shearing force.

Figure 17 visualizes the particle deformation and the flow field for six consecutive time instants. As the shear flow is induced by the moving plates, the shearing force is imposed on the solid particle, and causes the particle elongation toward the extensional direction. In the transient state during the development of the deformation, it is observed

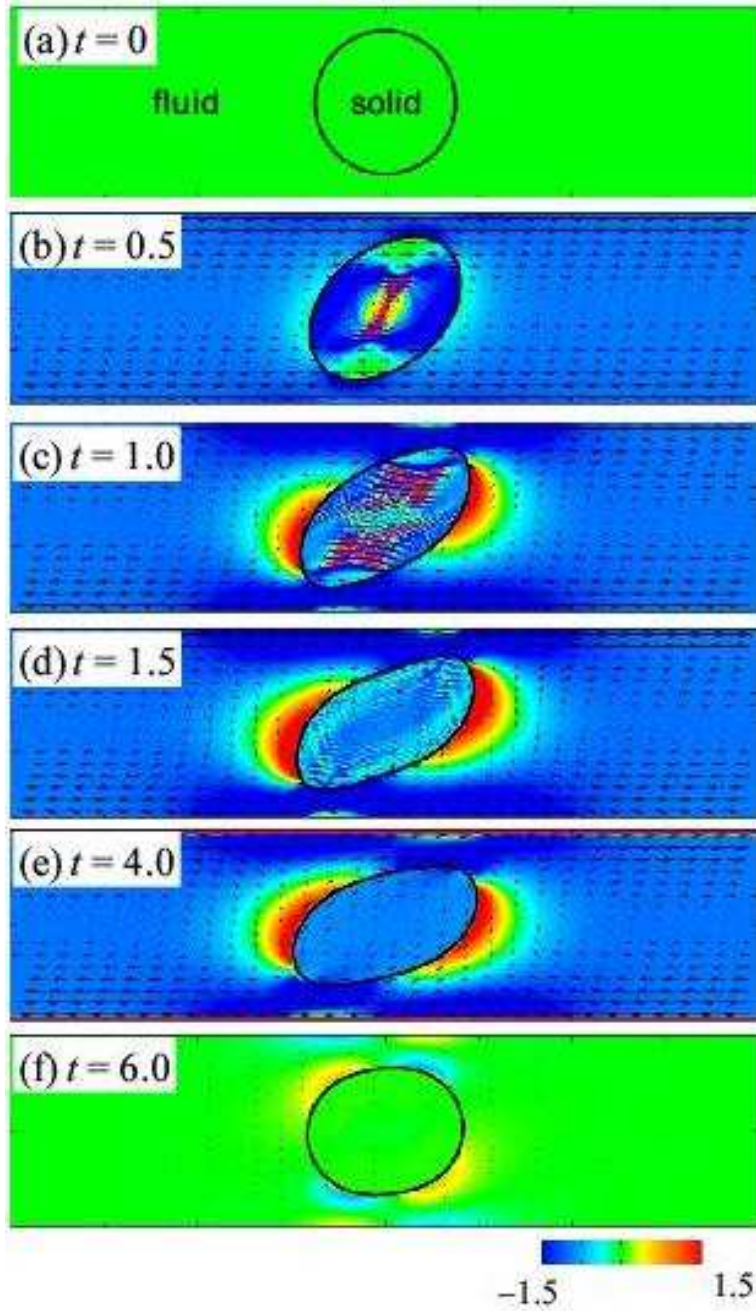


FIG. 17: Snapshots of the velocity (arrows) and vorticity (color) fields involving a circular particle in the imposing-releasing shear flow between two parallel plates. The number of grid points is 1024×256 . The upper and lower plates move at speed of 1 and -1 within a period of $t \in [0, 4]$, and then stop after $t = 4$. The solid obeys an incompressible Saint Venant-Kirchhoff law with $\mu_s = 0$, $\lambda_{\text{Lamé}}^s = 6$ and $\mu_{\text{Lamé}}^s = 4$.

in figure 17(b)(c) that the transverse elastic waves travel inside the solid, and are reflected by the fluid-structure interface. The wave amplitude is damped through the repetitious reflections with time as shown in figure 17(d)(e). As examined in [12], the elastic wave propagation inside the particle may play an important role on the deformation. As shown in figure 17(e), the vorticity inside the particle at $t = 4$ is negative, indicating that the particle experiences a tank-treading like motion. After the shearing force is released by setting the wall velocities to be zero at $t = 4$, the fluid flow rapidly decays and the deformed particle gradually recovers the circular shape. At $t = 6$ as shown in figure 17(f), the vorticity in the bulk fluid is almost zero, while the non-zero vorticity forms near the fluid-structure

interface, indicating the particle shape is under recovery.

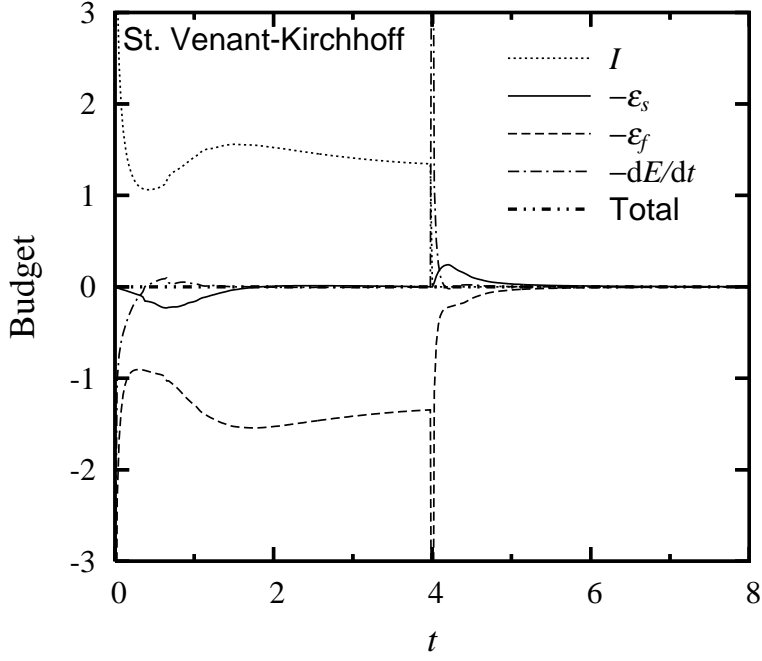


FIG. 18: The budget of the kinetic-energy transport (60) in the imposing-releasing shear flow. The conditions are the same as those of figure 17. The dotted, solid, dashed, and dashed-dotted curves correspond to the energy input rate \mathcal{I} , the strain energy rate $-\varepsilon_s$, the energy dissipation rate $-\varepsilon_f$, and the kinetic-energy transport $-dE/dt$, respectively. The each component is provided in (61). The dashed-double-dotted curve corresponds to the summation of the left-hand-side terms of (60).

The complete recovery in the particle shape is established when the hyperelastic strain energy potential returns to the initial state. Therefore, the energy transfer between the fluid and solid phases is relevant to it. We here check whether the energy transport is numerically conserved during the simulation. In the system addressed in this section, the budget of the kinetic-energy transport is written as

$$\mathcal{I} - \varepsilon_s - \varepsilon_f - \frac{dE}{dt} = 0, \quad (60)$$

where \mathcal{I} , ε_s , ε_f , and E , respectively, denote averaged quantities of the energy input rate, the strain energy rate, the energy dissipation rate, and the kinetic-energy, expressed as

$$\begin{aligned} \mathcal{I} &= \frac{\mu_f}{L_y} \left(V_W^{\text{upper}} \left\langle \frac{\partial v_x}{\partial y} \right\rangle_{\Gamma_W^{\text{upper}}} - V_W^{\text{lower}} \left\langle \frac{\partial v_x}{\partial y} \right\rangle_{\Gamma_W^{\text{lower}}} \right), \\ \varepsilon_s &= \langle \phi_s \mathbf{D}' : \boldsymbol{\sigma}'_s \rangle_{\Omega}, \\ \varepsilon_f &= 2\mu_f \langle (1 - \phi_s) \mathbf{D}' : \mathbf{D}' \rangle_{\Omega}, \\ E &= \frac{\rho}{2} \langle \mathbf{v} \cdot \mathbf{v} \rangle_{\Omega}, \end{aligned} \quad (61)$$

where $\langle \dots \rangle_{\Gamma_W}$ stands for the average over the wall, and $\langle \dots \rangle_{\Omega}$ for the average over the entire domain Ω . Figure 18 shows the time history of the each contribution in the left-hand-side of (60). As the flow evolves, the particle deforms, and thereby the particle stores the strain energy as indicated by the solid curve with negative value in figure 18. After the walls stop at $t = 4$, the particle releases the strain energy. The double-chained curve in figure 18 shows the summation of the left-hand-side terms of (60). Its absolute value, corresponding to the numerical error, is less than 10^{-5} , which is much smaller than the variation of the contributions of the individual terms. The system is well conserved during the simulation in view of the energy balance, because the equality of (60) is almost fulfilled. It is important to emphasize that the numerical energy conservation hinges upon the finite difference schemes, and the method proposed by Kajishima [38] is employed in the present study.

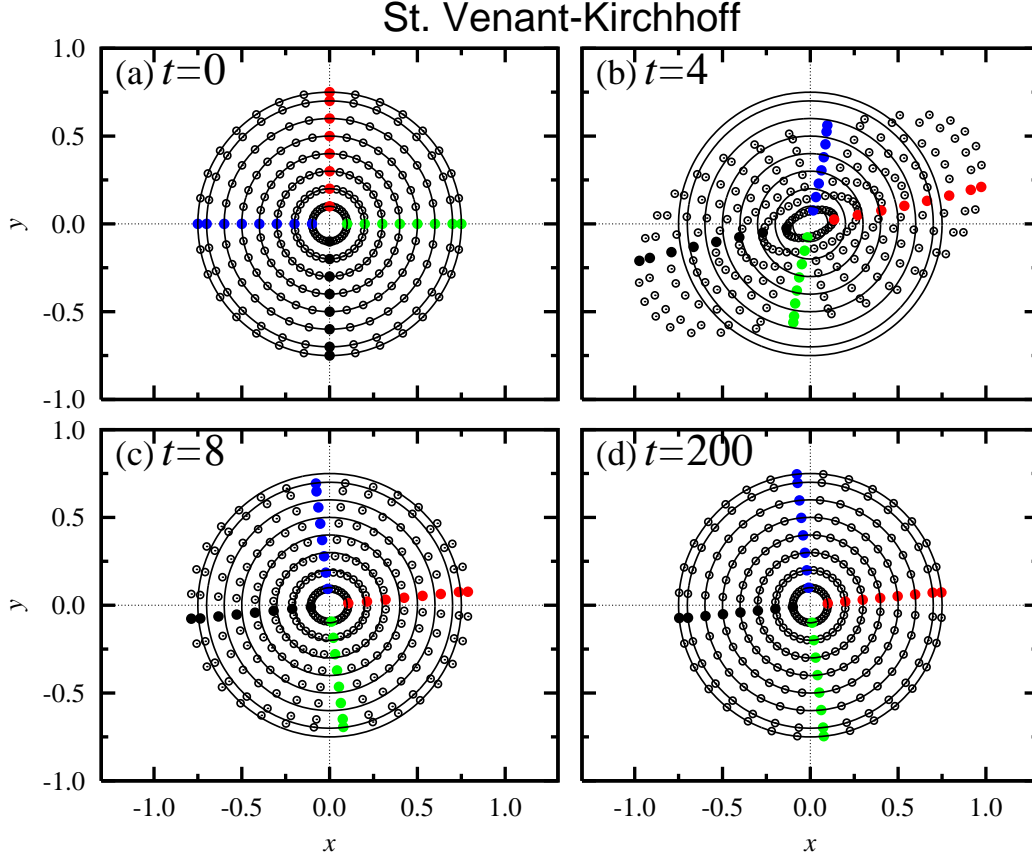


FIG. 19: Material point distribution in the imposing-releasing shear flow involving a circular particle between two parallel plates with the 1024×256 mesh. The conditions are the same as those of figure 17. The colored filled circles are distributed to demonstrate the rotation.

To directly demonstrate whether the reversibility can be captured, the distributions of the tracers for four consecutive time instants are shown in figure 19. As depicted in figure 19(a), the tracers are initially seeded on the concentric circles inside the solid to demonstrate the local displacements inside the solid. The bilinear interpolation to the tracer location is applied to identifying its velocity, and its position is temporally updated in a Lagrangian way. Figure 19(b) shows the tracer distribution at the most deformed instant $t = 4$ when the particle is under the tank-treading like motion. After the wall velocities is set to be zero at $t = 4$, the tracer particles gradually move back toward the initial concentric circles with time. It should be noted that because the degree of freedom corresponding to the rigid rotation is allowed, the tracer distributions in figure 19(c)(d) turn in the clockwise directions about 80 degrees with respect to the initial distribution in figure 19(a). At the instant $t = 8$, when the same period as the shear-imposing stage (four unit time) has elapsed after the walls stop, the discrepancy between the tracer location and the concentric circle is clearly shown in figure 19(c), indicating that the recovery in the particle shape is still underway. After a sufficiently long time ($t = 200$), the tracers are found to be back in the concentric circles as shown in figure 19(d). We may say that the present Eulerian approach can capture the reversibility in shape under certain right circumstances, which will be discussed later.

To assess the effect of the spatial resolution, the outlines of the fluid-structure interface, which are identified as the isolines at $\phi_s = 1/2$, for various number of grid points for different materials are shown in figure 20. As the spatial resolution is increased, the deformed shape more settles to a convergent curve at the instant $t = 4$ when the particle exhibits the most deformed shape, and the outline at $t = 200$ shows better recovery to the initial curve at $t = 0$.

To further assess the grid convergence behavior in the particle deformation, the deformation mode is here investigated. As explained in §IV B 1, the deformation modes are determined using (54), (55) and (58). Due to the symmetry of the system, the odd-number-order modes $R_{c,2n+1}$ and $R_{s,2n+1}$ are identically zero. Temporal evolutions of the modal amplitudes $|R_n|$ ($n = 0, 2, 4$ and 4) of the particle deformation for various number of grid points are shown in figure 21 (for the linear Mooney-Rivlin material) and in figure 22 (for the incompressible Saint Venant-Kirchhoff material). Both figure 21 and figure 22 demonstrate the convergence behavior of the profiles with increasing

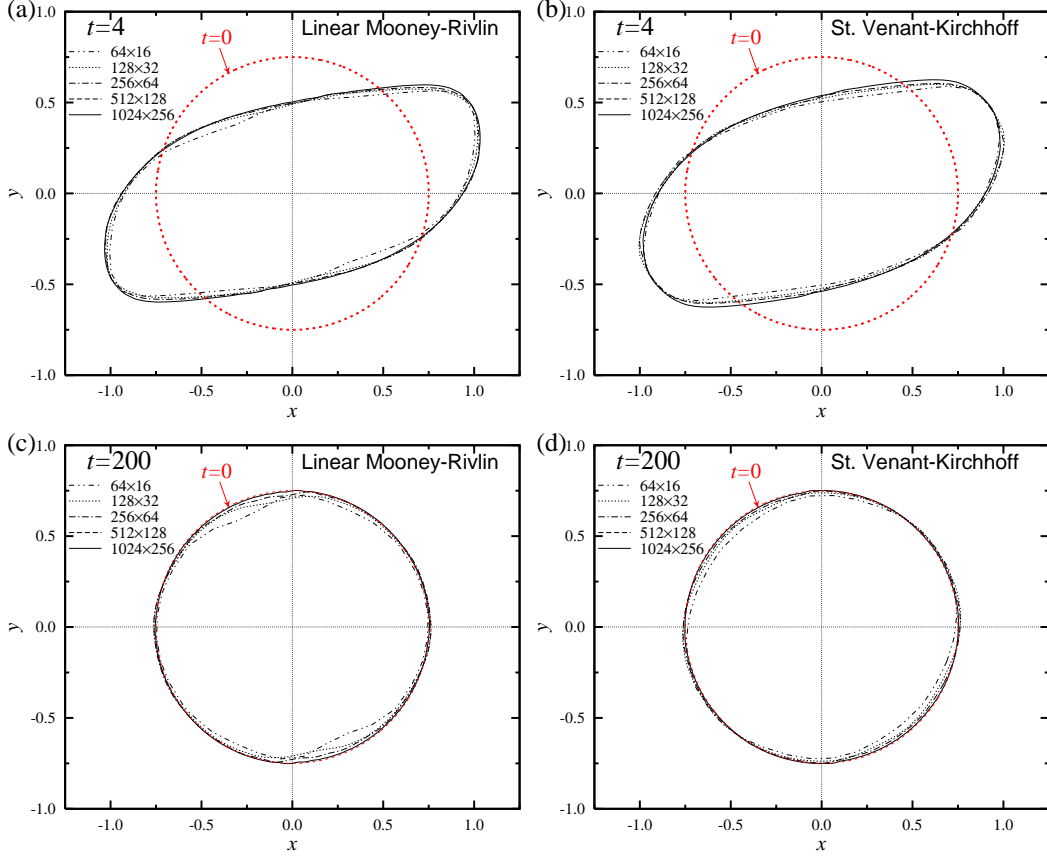


FIG. 20: Outlines of the fluid-structure interface in the imposing-releasing shear flow involving a circular particle between two parallel plates for various number of grid points ($N_x \times N_y = 64 \times 16$, 128×32 , 256×64 , 512×128 and 1024×256). The imposing-releasing shear scheme, the geometry, and the fluid properties are the same as those of figure 17. The left panels: the linear Mooney material with $\mu_s = 0$, $c_1 = 4$, $c_2 = 2$ and $c_3 = 0$. The right panels: the incompressible Saint Venant-Kirchhoff material with $\mu_s = 0$, $\lambda_{\text{Lamé}}^s = 6$ and $\mu_{\text{Lamé}}^s = 4$. The upper panels: at $t = 4$. The lower panels: at $t = 200$.

the number of grid points. After the walls stop at $t = 4$, the zeroth-order mode $|R_0|$ approaches 0.75, corresponding to the unstressed radius, in the case of the spatial resolution $N_x \times N_y = 256 \times 64$ or higher. However, the higher-order amplitudes $|R_2|$, $|R_4|$ and $|R_6|$ at the fully developed stage obviously settle to some non-zero values. This tendency is more pronounced in the lower grid resolution, indicating that some spurious deformation remains. However, the deviation from zero for $|R_n|$ ($n \neq 0$) vanishes exponentially as the spatial resolution is increased.

To quantify the spurious residual deformation, the modal amplitudes $|R_n|$ ($n = 2, 4$ and 6) at $t = 200$ as a function of the number of grid points are plotted in figure 23. The residual amplitudes are nearly proportional to N_x^{-1} , indicating the first-order accuracy in capturing unstressed shape. As demonstrated in §IV A for the much simpler system consisting of the fluid-structure layers, the present fluid-structure coupling method involves the first-order accuracy, which is also reflected on the grid convergence of the reversibility in shape.

2. Shape reversibility of a rectangular particle

We also perform a reversibility test for a rectangular particle with a dimension of 2.375×1 to demonstrate the applicability of the method to an object with a larger aspect ratio and sharp corners. The initial setup is depicted in figure 24(a). Figure 24 visualizes the particle deformation and the velocity and vorticity fields for six consecutive time instants. Similar to the system involving the circular particle in figure 17, the elastic wave propagation and its attenuation are observed in figure 24(b)(c)(d). However, unlike the tank-treading motion in figure 17(e), the vorticity inside the particle at $t = 4$ is not entirely negative in figure 24(e), indicating that the particle does not experience the tank-treading or tumbling motion. It is because the rotational motion is geometrically suppressed due to the hydrodynamic interaction between the particle and the wall. As shown in figure 24(e), the left-top and right-bottom

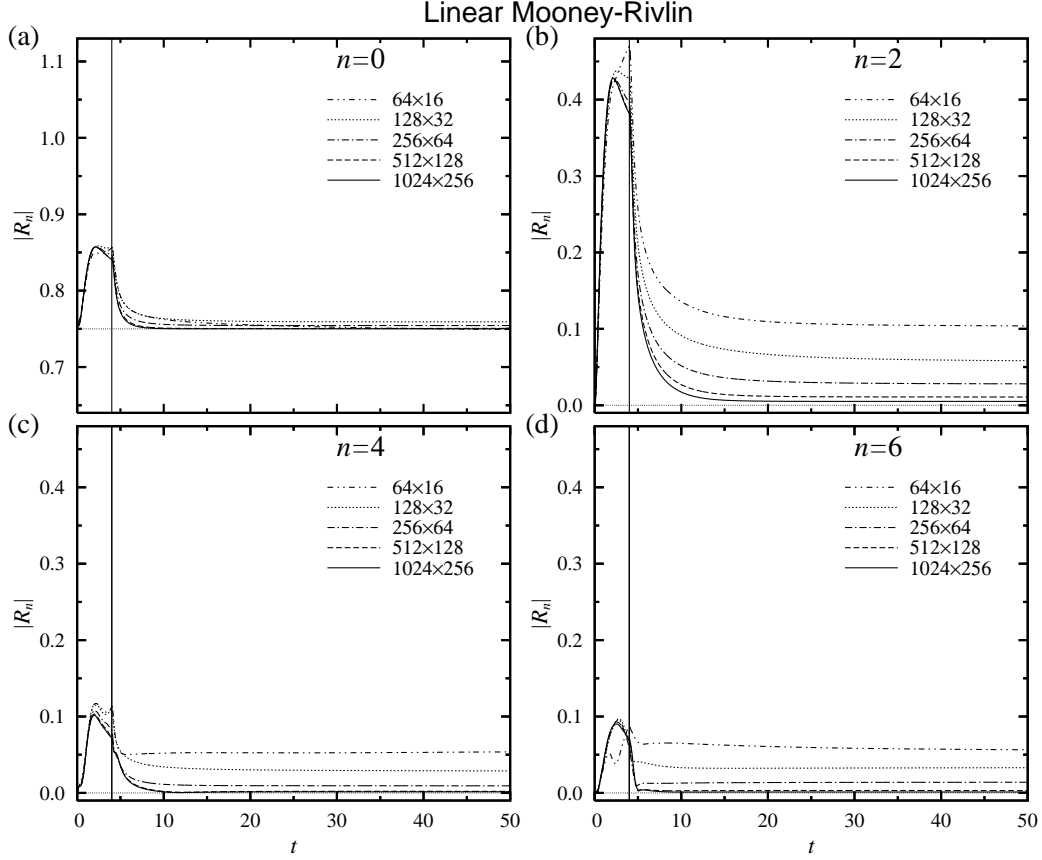


FIG. 21: Time history of the n -th order modal amplitude $|R_n|$ of the particle deformation in the imposing-releasing shear flow involving a circular particle between two parallel plates for various number of grid points ($N_x \times N_y = 64 \times 16, 128 \times 32, 256 \times 64, 512 \times 128$ and 1024×256). (a) $n = 0$, (b) $n = 2$, (c) $n = 4$, and (d) $n = 6$. The solid obeys a linear Mooney-Rivlin law with $\mu_s = 0$, $c_1 = 4$, $c_2 = 2$ and $c_3 = 0$.

corners of the object are largely deformed. From the subsequent results on the shape reversibility in figure 26 and the grid convergence behavior in figure 27, we strongly envisage that large deformations are resulted from the physical mechanism, not induced by numerical errors. After the shearing force is released at $t = 4$, the deformed particle gradually recovers the unstressed shape as shown in figure 24(f) ($t = 6$).

Figure 25 shows the budget of the kinetic energy transport. Similar to the results in figure 18, the numerical error is much smaller than the variation of the contributions of the individual terms in (60), indicating that the energy exchange between the fluid and solid phases via the solid deformation is reasonably guaranteed.

Figure 26 shows the tracer distributions for four consecutive time instants. After the particle well deforms at $t = 4$, the recovery of the material points toward the initial configuration is demonstrated. Even though the rotational motion of the particle is suppressed, the object at fully developed state in figure 26(d) slightly turns in the clockwise direction as compared with the initial distribution in figure 26(a). It would be remarkable to note that, though the left-top and right-bottom corners of the object are strongly stretched at $t = 4$, the object gradually resumes the shape of the original corners as the time goes on.

Figure 27 shows the outlines of the fluid-structure interface for various number of grid points and different materials. The edges of the rectangle are obviously smeared out, which would be the inevitable effect of the numerical dissipation involved in the fifth-order WENO scheme, which is applied to updating ϕ_s . Nevertheless, similar to figure 20, with increasing the number of grid points, the particle shapes at $t = 4$ and $t = 200$ converge, and the reversibility in shape can be better attained.

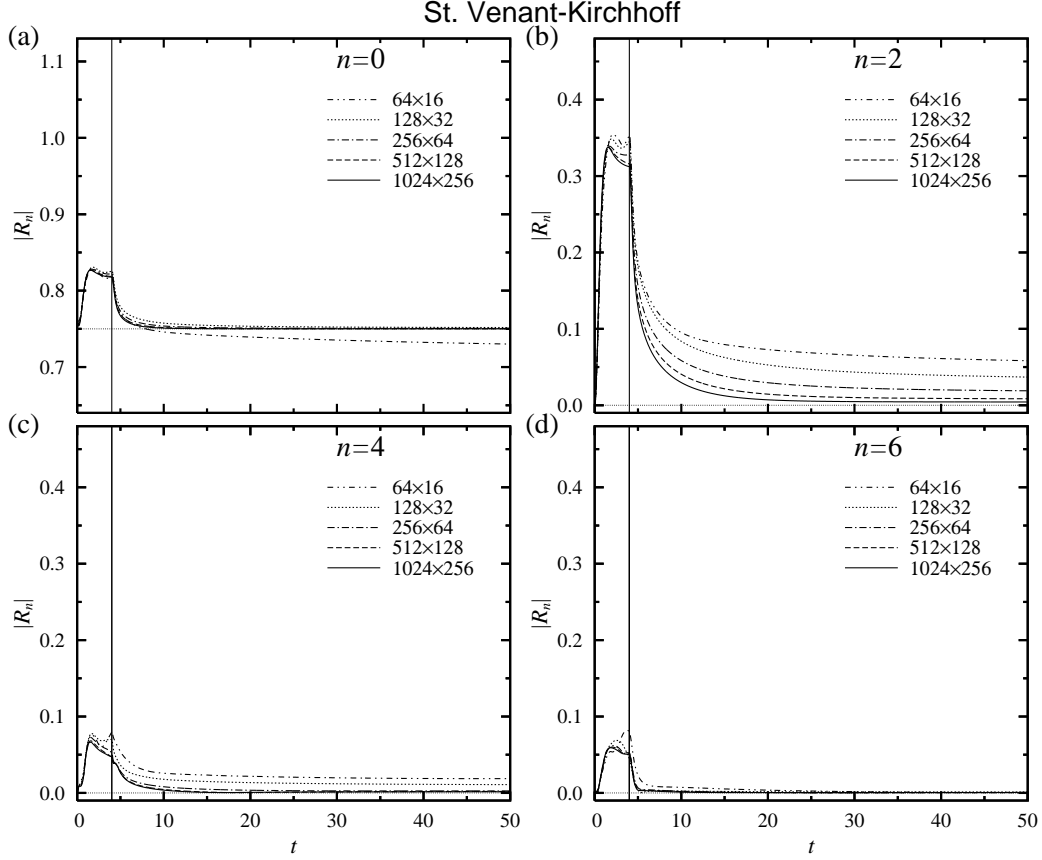


FIG. 22: Same as figure 21, but the solid obeys an incompressible Saint Venant-Kirchhoff law with $\mu_s = 0$, $\lambda_{\text{Lamé}}^s = 6$ and $\mu_{\text{Lamé}}^s = 4$.

V. CONCLUSION AND PERSPECTIVES

A full Eulerian simulation method for solving Fluid-Structure Interaction (FSI) problems has been developed. A volume-of-fluid formulation [23] was applied to describing the multi-component geometry. The temporal change in the solid deformation was described in the Eulerian frame by updating a left Cauchy-Green deformation tensor, which was used to express the nonlinear Mooney-Rivlin constitutive law. The validity of the present simulation method was established through comparisons with the analytical solution of the oscillatory response in fluid-solid parallel layers, and also with the available simulation data of the solid motion in the lid-driven cavity flow [97] and the two-particle interaction in the Couette flow [12]. We confirmed that the present Eulerian approach can capture the reversibility in shape as long as the grid resolution is sufficiently high. Further, we demonstrated that the numerical accuracy due to the fluid-structure coupling is of the first-order with respect to the grid size.

The significance of the present full Eulerian simulation method may be that the approach showed a feasibility of reducing the FSI coupling problem to a simple incompressible fluid flow solvers. Thus, the conventionally-used efficient computational techniques, such as the fast Fourier transform, and multi-grid method, are applicable. The present Eulerian method is proved to be well-suited for using the voxel-based multi-component geometry on the fixed Cartesian system. Once the initial field of the solid volume fraction is given over the entire domain, the present Eulerian method enables one to carry out the FSI simulation without mesh generation procedure. The method promises to extend the possibility of the FSI simulation to certain additional classes of problems in the medical field, owing to a facility in incorporating the voxel data directly converted from medical images. The practical demonstration is the future subject of the present authors.

To improve the accuracy in the present fluid-structure coupling to a level available for practical applications, it is important to capture the interface more sharply. We now use the fifth-order WENO method for advecting the solid volume fraction field, which temporally makes the interface numerically diffusive. As frequently used in the multiphase flow simulation, to suppress the numerical diffusion, elaborated techniques for the sharp interface advection such as

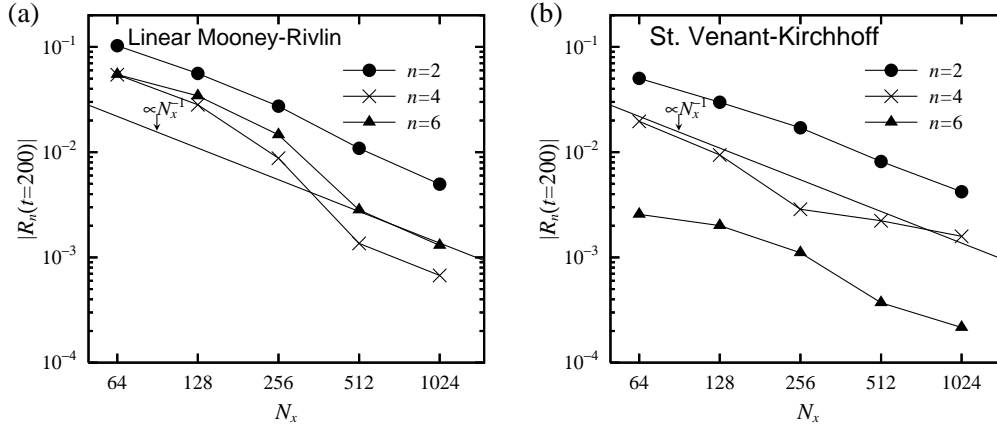


FIG. 23: Residual modal amplitudes $|R_n|$ of the particle deformation at $t = 200$ versus the number N_x of grid points in the imposing-releasing shear flow. (a): for the results in figure 21 employing the linear Mooney-Rivlin material (b): for the results in figure 22 employing the incompressible Saint Venant-Kirchhoff material.

SLIC [52], PLIC [17, 89], and THINC [86] methods would be applicable. As an alternative of the VOF function, the level set function [56, 64] is another option. On the dynamic interaction, we now write the stress in a fluid-structure mixture form. Although the strain rate has a discontinuity across the fluid-structure interface, it is smoothed out at the grid scale in the present simulation method. The ideas of the immersed interface treatment [41, 42] and the localized strain formulation [53] would be effective to improve the accuracy in the fluid-structure coupling. It is a challenging task to overcome the multiphysics difficulty particularly associated with the difference in constitutive laws for fluid and solid. Improved accuracy in capturing the interface and robust time advancement [32, 33] are the ongoing subject of the present authors.

Acknowledgments

The authors thank Toshiaki Hisada, Robert M. Miura, Huaxiong Huang, Lucy T. Zhang, Yoichiro Mori, Shigeho Noda, Teruo Matsuzawa, Hiroshi Okada, and Shigenobu Okazawa for fruitful discussions. K.S. is grateful to Tong Gao for providing the detailed simulation conditions in §IV B 2. The authors thank the referees for their useful comments and suggestions. This research was supported by Research and Development of the Next-Generation Integrated Simulation of Living Matter, a part of the Development and Use of the Next-Generation Supercomputer Project of the Ministry of Education, Culture, Sports, Science and Technology (MEXT), and by the Grant-in-Aid for Young Scientist (B) (No.21760120) of MEXT.

-
- [1] Amsden, A.A. and Harlow, F.H., “A simplified MAC technique for incompressible fluid flow calculations,” J. Comput. Phys., **6**, (1970) pp. 322–325.
 - [2] Bazilevs, Y., Calo, V.M., Zhang, Y. and Hughes, T.J.R., “Isogeometric fluid-structure interaction analysis with applications to arterial blood flow,” Comput. Mech., **38**, (2006) pp. 310–322.
 - [3] Belytschko, T., “Fluid-structure interaction,” Comput. Structure, **12**, (1980) pp. 459–469.
 - [4] Bonet, J. and Wood, R.D., ‘*Nonlinear Continuum Mechanics for Finite Element Analysis*,’ (2008) Chap. 4 (Cambridge University Press, Cambridge, second edition).
 - [5] Canuto, C., Hussaini, M.Y., Quarteroni, A. and Zang, T.A., ‘*Spectral Methods in Fluid Dynamics*,’ (1988) Chap.4 (Springer-Verlag, New York).
 - [6] Chang, Y.C., Hou, T.Y., Merriman, B. and Osher, S., “A level set formulation of Eulerian interface capturing methods for incompressible fluid flows,” J. Comput. Phys., **124**, (1996) pp. 449–464.
 - [7] Chen, J.-S. and Pan, C., “A pressure projection method for nearly incompressible rubber hyperelasticity, Part I: Theory,” Trans. ASME J. Appl. Mech., **63**, (1996) pp. 862–868.
 - [8] Cottet, G.-H., Maitre, E. and Milcent, T., “Eulerian formulation and level set models for incompressible fluid-structure interaction,” Math. Modelling and Numer. Anal. **42**, (2008), pp. 471–492.

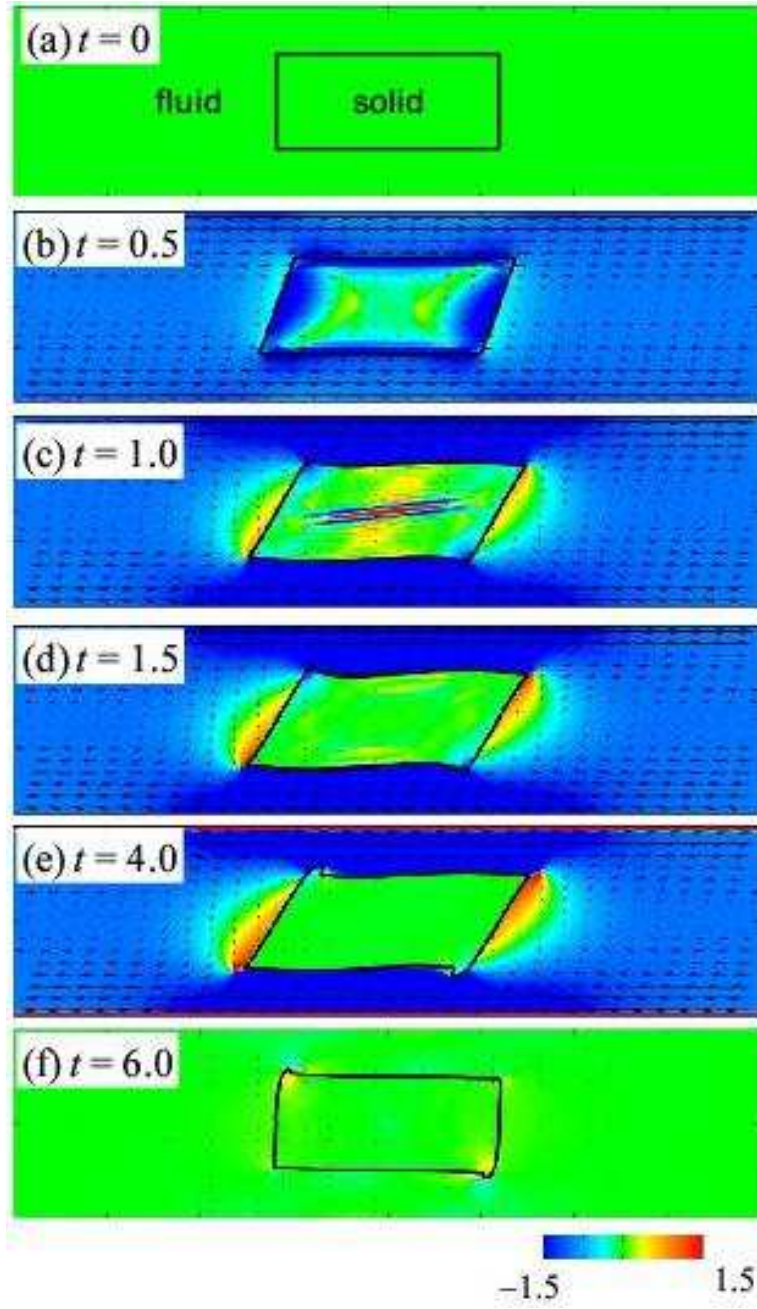


FIG. 24: Snapshots of the velocity (arrows) and vorticity (color) fields in the imposing-releasing shear flow involving a rectangular particle between two parallel plates. The number of grid points is 1024×256 . The upper and lower plates move at speeds of 1 and -1 within a period of $t \in [0, 4]$, and then stop after $t = 4$. The solid obeys an incompressible Saint Venant-Kirchhoff law with $\mu_s = 0$, $\lambda_{\text{Lamé}}^s = 6$ and $\mu_{\text{Lamé}}^s = 4$.

- [9] Dunne, T., “An Eulerian approach to fluid-structure interaction and goal-oriented mesh adaptation,” *Int. J. Numer. Meth. Fluids*, **51**, (2006) pp. 1017-1039.
- [10] Eggleton, C.D. and Popel, A.S., “Large deformation of red blood cell ghosts in a simple shear flow,” *Phys. Fluids*, **10**, (1998) pp. 1834-1845.
- [11] Figueroa, C.A., Vignon-Clemental, I.E., Jansen, K.E., Hughes, T.J.R. and Taylor, C.A., “A coupled momentum method for modeling blood flow in three-dimensional deformable arteries,” *Comput. Methods Appl. Mech. Eng.*, **195**, (2006) pp. 5685-5706.
- [12] Gao, T. and Hu, H.H., “Deformation of elastic particles in viscous shear flow,” *J. Comput. Phys.*, **228**, (2009) pp. 2132-2151.

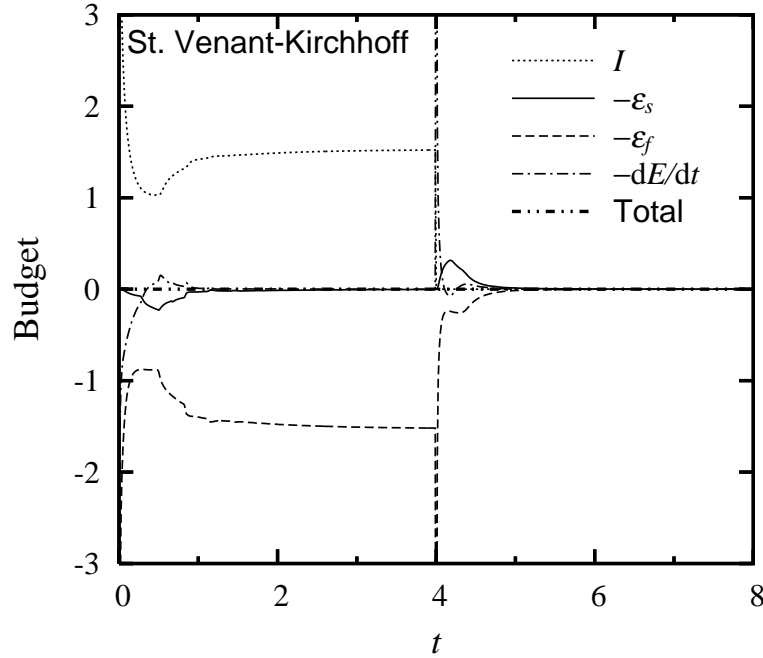


FIG. 25: The budget of the kinetic-energy transport (60) in the imposing-releasing shear flow. The conditions are the same as those of figure 24. The dotted, solid, dashed, and dashed-dotted curves correspond to the energy input rate \mathcal{I} , the strain energy rate $-\varepsilon_s$, the energy dissipation rate $-\varepsilon_f$, and the kinetic-energy transport $-dE/dt$, respectively. The each component is provided in (61). The dashed-double-dotted curve corresponds to the summation of the left-hand-side terms of (60).

- [13] Gil, A.J., “Structural analysis of prestressed Saint Venant-Kirchhoff hyperelastic membranes subjected to moderate strains,” *Comput. and Structures*, **84**, (2006) pp. 387–411.
- [14] Glowinski, R., Pan, T.-W., Hesla, T.I. and Joseph, D.D., “A distributed Lagrange multiplier/fictitious domain method for particulate flows,” *Int. J. Multiphase Flow*, **25**, (1999) pp. 755–794.
- [15] Glowinski, R., Pan, T.-W., Hesla, T.I., Joseph, D.D. and P eriaux, J., “A fictitious domain approach to the direct numerical simulation of incompressible viscous flow past moving rigid bodies: application to particulate flow,” *J. Comput. Phys.*, **169**, (2001) pp. 363–426.
- [16] Gong, X., Sugiyama, K., Takagi, S. and Matsumoto, S., “The deformation behavior of multiple red blood cells in a capillary vessel,” *J. Biomech. Eng.*, **131**, (2009) 074504.
- [17] Gueyffier, D., Li, J., Nadim, A., Scardovelli, R. and Zaleski, S., “Volume-of-Fluid interface tracking with smoothed surface stress methods for three-dimensional flows,” *J. Comput. Phys.*, **152**, (1999) pp. 423–456.
- [18] G ltop, T., “On the propagation of acceleration waves in incompressible hyperelastic solids,” *J. Sound and Vibration*, **264**, (2003) pp. 377–389.
- [19] Gurtin, M.E. and Guidugli, P.P., “The thermodynamics of constrained materials,” *Arch. Rational Mech. Anal.*, **51**, (1973) pp. 192–208.
- [20] Hamamoto, M., Hisada, T. and Suzumori, K., “Feasibility study of an electrostatic actuator by finite element interaction analysis,” *Int. J. Appl. Electromagnetics and Mech.*, **10**, (1999) pp. 249–257.
- [21] Harlow, F.H. and Welch, J.E., “Numerical calculation of time-dependent viscous incompressible flow of fluid with free surface,” *Phys. Fluids*, **8**, (1965) pp. 2182–2189.
- [22] Hirt, C.W., Amsden, A.A. and Cook, J.L., “An arbitrary Lagrangian-Eulerian computing method for all flow speeds,” *J. Comput. Phys.*, **14**, (1974) pp. 227–253.
- [23] Hirt, C.W. and Nichols, B.D., “Volume of fluid (VOF) method for the dynamics of free boundaries,” *J. Comput. Phys.*, **39**, (1981) pp. 201–225.
- [24] Hisada, T., ‘*Foundations of Tensor Analysis for Nonlinear Finite Element Method*,’ (1992) Chaps. 2 and 5 (in Japanese, Maruzen).
- [25] Hu, H.H., “Direct simulation of flows of solid-liquid mixtures,” *Int. J. Multiphase Flow*, **22**, (1996) pp. 335–352.
- [26] Huang, H., Sugiyama, K. and Takagi, S., “An immersed boundary method for restricted diffusion with permeable interfaces,” *J. Comput. Phys.*, **228**, (2009) pp. 5317–5322.
- [27] Huang, W.-X. and Sung, J., “An immersed boundary method for fluid-flexible structure interaction,” *Comput. Methods Appl. Mech. Eng.*, **198**, (2009) pp. 2650–2661.
- [28] Huerta, A. and Liu, W.K., “Viscous flow with large free surface motion,” *Comput. Methods Appl. Mech. Eng.*, **69**, (1988)

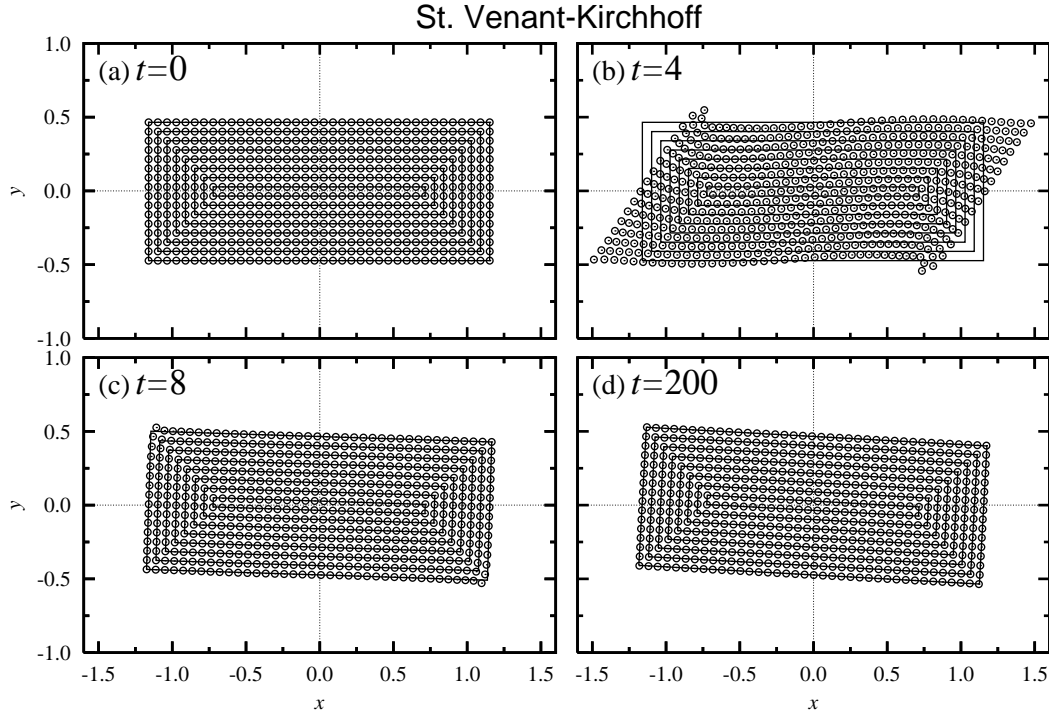


FIG. 26: Material point distribution in the imposing-releasing shear flow involving a rectangular particle between two parallel plates. with the 1024×256 mesh. The conditions are the same as those of figure 24.

pp. 277–324.

- [29] Huerta, A. and Liu, W.K., “Viscous flow structure interaction,” *Trans. ASME J. Pressure Vessel Tech.*, **110**, (1988) pp. 15–21.
- [30] Hughes, T.J.R., Liu, W.K. and Zimmermann, T.K., “Lagrangian-Eulerian finite element formulation for incompressible viscous flows,” *Comput. Methods Appl. Mech. Eng.*, **29**, (1981) pp. 329–349.
- [31] Hughes, T.J.R. and Stewart, J.R., “A space-time formulation for multiscale phenomena,” *J. Comput. Appl. Math.*, **74**, (1996) pp. 217–229.
- [32] Ii, S., Sugiyama, K., Takeuchi, S., Takagi, S. and Matsumoto, Y., “Development of accurate numerical model for the fluid-structure interaction problem based on Eulerian framework,” *Proc. of 10th US National Cong. on Comput. Mech.*, Ohio, USA, (2009) No. 158294.
- [33] Ii, S., Sugiyama, K., Takeuchi, S., Takagi, S. and Matsumoto, Y., “An implicit full Eulerian method for the fluid-structure interaction problem,” *Int. J. Numer. Meth. Fluids*, (2010) (accepted).
- [34] Ikeno, T. and Kajishima, T., “Finite-difference immersed boundary method consistent with wall conditions for incompressible turbulent flow simulations,” *J. Comput. Phys.*, **226**, (2007) pp. 1485–1508.
- [35] Jacqmin, D., “Calculation of two-phase Navier-Stokes flows using phase-field modeling,” *J. Comput. Phys.*, **155**, (1999) pp. 96–127.
- [36] Jiang, G.-S. and Shu, C.-W., “Efficient implementation of weighted ENO scheme,” *J. Comput. Phys.*, **126**, (1996) pp. 202–228.
- [37] Johnson, A.A. and Tezduyar, T.E., “3D simulation of fluid-particle interactions with the number of particles reaching 100,” *Comput. Methods Appl. Mech. Eng.*, **145**, (1997) pp. 301–321.
- [38] Kajishima, T., “Conservation properties of finite difference method for convection,” *Trans. Jpn. Soc. Mech. Eng. B*, **60**-574, (1994) pp. 2058–2063 (in Japanese).
- [39] Kajishima, T. and Takiguchi, S., “Interaction between particle clusters and particle-induced turbulence,” *Int. J. Heat and Fluid Flow*, **23**, (2002) pp. 639–646.
- [40] Kajishima, T., Takiguchi, S., Hamasaki, H. and Miyake, Y., “Turbulence structure of particle-laden flow in a vertical plane channel due to vortex shedding,” *JSME Int. J. Ser. B*, **44**, (2001) pp. 526–535.
- [41] LeVeque, R.J. and Li, Z., “The immersed interface method for elliptic equations with discontinuous coefficients and singular sources,” *SIAM J. Numerical Analysis*, **31**, (1994) pp. 1019–1044.
- [42] Li, Z. and Ito, K., ‘*The Immersed Interface Method*,’ (2006) (SIAM, Philadelphia).
- [43] Li, Z. and Lai, M.-C., “The immersed interface method for the Navier-Stokes equations with singular forces,” *J. Comput. Phys.*, **171**, (2001) pp. 822–842.
- [44] Liu, W.K., Liu, Y., Farrell, D., Zhang, L., Wang, X.S., Fukui, Y., Patankar, N., Zhang, Y. and Bajaj, C., “Immersed

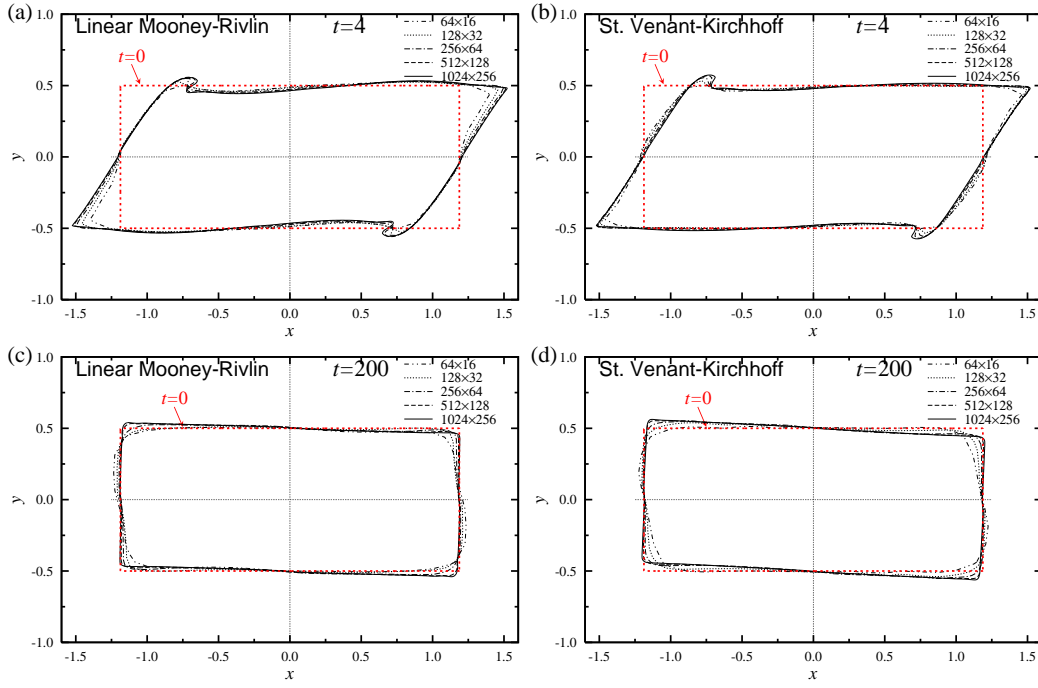


FIG. 27: Outlines of the fluid-structure interface in the imposing-releasing shear flow involving a rectangular particle between two parallel plates for various number of grid points ($N_x \times N_y = 64 \times 16$, 128×32 , 256×64 , 512×128 and 1024×256). The imposing-releasing shear scheme, the geometry, and the fluid properties are the same as those of figure 24. The left panels: the linear Mooney material with $\mu_s = 0$, $c_1 = 4$, $c_2 = 2$ and $c_3 = 0$. The right panels: the incompressible Saint Venant-Kirchhoff material with $\mu_s = 0$, $\lambda_{\text{Lamé}}^s = 6$ and $\mu_{\text{Lamé}}^s = 4$. The upper panels: at $t = 4$. The lower panels: at $t = 200$.

- finite element method and its applications to biological systems,” Comput. Methods Appl. Mech. Eng., **195**, (2006) pp. 1722–1749.
- [45] Liu, X.-D., Osher, S. and Chan, T., “Weighted essentially non-oscillatory schemes,” J. Comput. Phys., **115**, (1994) pp. 200–212.
- [46] Liu, C. and Walkington, N.J., “An Eulerian description of fluids containing visco-elastic particles,” Arch. Rational Mech. Anal., **159**, (2001) pp. 229–252.
- [47] Matsunaga, N., Liu, H. and Himeno, R., “An image-based computational fluid dynamics method for haemodynamic simulation,” JSME Int. J. Ser. C, **45**, (2002) pp. 989–996.
- [48] Mooney, M., “A theory of large elastic deformation,” J. Appl. Phys., **11**, (1940) pp. 582–592.
- [49] Mori, Y. and Peskin, C.S., “Implicit second-order immersed boundary methods with boundary mass,” Comput. Methods Appl. Mech. Eng., **197**, (2008) pp. 2049–2067.
- [50] Nitikitpaiboon, C. and Bathe, K.J., “An arbitrary Lagrangian-Eulerian velocity potential formulation for fluid-structure interaction,” Comput. and Structures, **47**, (1993) pp. 871–891.
- [51] Noda, S., Fukasaku, K. and Himeno, R., “Blood flow simulator using medical images without mesh generation,” IFMBE Proc. of World Cong. on Medical Physics and Biomedical Engineering 2006, Seoul, Korea, (2006) pp. 36–40.
- [52] Noh, W.F. and Woodward, P.R., “SLIC (simple line interface calculation),” Lecture Notes in Phys., **59**, (1976) pp. 330–340.
- [53] Okada, H. and Atluri, S.N., “Embedded localized strain zone constitutive model in finite strain and finite rotation,” Proc. of Int. Conf. on Computational Engineering Science, **2**, (1995) pp. 2154–5159.
- [54] Okazawa, S., Kashiwayama, K. and Kaneko, Y., “Eulerian formulation using stabilized finite element method for large deformation solid dynamics,” Int. J. Numer. Meth. Eng., **72**, (2007) pp. 1544–1559.
- [55] Osher, S. and Fedkiw, R., “Level set methods: an overview and some recent results,” J. Comput. Phys., **169**, (2001) pp. 463–502.
- [56] Osher, S. and Fedkiw, R., ‘Level set methods and dynamic implicit surfaces,’ (2003) (Springer-Verlag, New York).
- [57] Peskin, C.S., “Flow patterns around heart valves: a numerical method,” J. Comput. Phys., **10**, (1972) pp. 252–271.
- [58] Peskin, C.S., “The immersed boundary method,” Acta Numerica, **11**, (2002) pp. 479–517.
- [59] Pozrikidis, C., “Effect of membrane bending stiffness on the deformation of capsules in simple shear flow,” J. Fluid Mech., **440**, (2001) pp. 269–291.
- [60] Pozrikidis, C., “Axisymmetric motion of a file of red blood cells through capillaries,” Phys. Fluids, **17**, (2005) 031503.
- [61] Rivlin, R.S., “Large elastic deformations of isotropic materials IV, Further development of general theory,” Phil. Trans. R. Soc. A, **241**, (1948) pp. 379–397.

- [62] Saad, Y. and Schultz, Y., "GMRES: a generalized minimal residual algorithm for solving nonsymmetric linear systems," *SIAM J. Sci. Stat. Comput.*, **7**, (1986) pp. 856–869.
- [63] Sawada, T. and Hisada, T., "Fluid-structure interaction analysis of the two-dimensional flag-in-wind problem by an interface-tracking ALE finite element method," *Comput. and Fluids*, **36**, (2007) pp. 136–146.
- [64] Sethian, J.A. and Smereka, P., "Level set methods for fluid interfaces," *Annu. Rev. Fluid Mech.*, **35**, (2003) pp. 341–372.
- [65] Shi, X. and Phan-Thien, N., "Distributed Lagrange multiplier/fictitious domain method in the framework of lattice Boltzmann method for fluid-structure interactions," *J. Comput. Phys.*, **206**, (2005) pp. 81–94.
- [66] Simo, J.C., Taylor, R.L. and Plesler, K.S., "Variational and projection methods for the volume constraint in finite deformation elasto-plasticity," *Comput. Methods Appl. Mech. Eng.*, **51**, (1985) pp. 177–208.
- [67] Skotheim, J.M. and Mahadevan, L., "Soft lubrication: The elastohydrodynamics of nonconforming and conforming contacts," *Phys. Fluids*, **17**, (2005) 092101.
- [68] Stein, K., Benney, R., Tezduyar, T. and Potvin, J., "Fluid-structure interactions of a cross parachute: numerical simulation," *Comput. Methods Appl. Mech. Eng.*, **191**, (2001), pp. 673–687.
- [69] Sugiyama, K., Ii, S., Takeuchi, S., Takagi, S. and Matsumoto, Y., "Full Eulerian simulations of biconcave neo-Hookean particles in a Poiseuille flow," *Comput. Mech.*, **46**, (2010) pp. 147–157.
- [70] Sussman, M., Smereka, P. and Osher, S., "A level set approach for computing solutions to incompressible two-phase flow," *J. Comput. Phys.*, **114**, (1994) pp. 146–159.
- [71] Takagi, S., Oguz, H.N. and Prosperetti, A., "PHYSALIS: a new method for particle simulation: part II: two-dimensional Navier-Stokes flow around cylinders," *J. Comput. Phys.*, **187**, (2003) pp. 371–390.
- [72] Takeuchi, S., Yuki, Y., Ueyama, A. and Kajishima, T., "A conservative momentum exchange algorithm for interaction problem between fluid and deformable particles," *Int. J. Numer. Meth. Fluids*, (2010) doi: 10.1002/fld.2272 (in print).
- [73] Tan, Z., Lim, K.M. and Khoo, B.C., "An immersed interface method for Stokes flows with fixed/moving interfaces and rigid boundaries," *J. Comput. Phys.*, **228**, (2009) pp. 6855–6881.
- [74] Taylor, C.A., Hughes, T.J.R. and Zarins, C.K., "Finite element modeling of blood flow in arteries," *Comput. Methods. Appl. Mech. Eng.*, **158**, (1998) pp. 155–196.
- [75] Tezduyar, T.E., Behr, M. and Liou, J., "A new strategy for finite element computations involving moving boundaries and interfaces - The deforming-spatial-domain/space-time procedure: I. The concept and the preliminary numerical tests," *Comput. Methods Appl. Mech. Eng.*, **94**, (1992) pp. 339–351.
- [76] Tezduyar, T.E., Behr, M. and Mittal, S., "A new strategy for finite element computations involving moving boundaries and interfaces - The deforming-spatial-domain/space-time procedure: II. Computations of free-surface flows, two-liquid flows, and flows with drifting cylinders," *Comput. Methods Appl. Mech. Eng.*, **94**, (1992) pp. 353–371.
- [77] Torii, R., Oshima, M., Kobayashi, T. and Takagi, K., "Numerical simulation system for blood flow in the cerebral artery using CT imaging data," *JSME Int. J. Ser. C*, **44**, (2001) pp. 982–989.
- [78] Torii, R., Oshima, M., Kobayashi, T., Takagi, K. and Tezduyar, T.E., "Influence of wall elasticity in patient-specific hemodynamics simulations," *Comput. and Fluids*, **36**, (2007) pp. 160–168.
- [79] Torii, R., Oshima, M., Kobayashi, T., Takagi, K. and Tezduyar, T.E., "Fluid-structure interaction modeling of a patient-specific cerebral aneurysm: influence of structural modeling," *Comput. Mech.*, **43**, (2008) pp. 151–159.
- [80] Trapp, J.A., "Reinforced materials with thermo-mechanical constraints," *Int. J. Eng. Sci.*, **9**, (1971) pp. 757–773.
- [81] Tryggvason, G., Sussman, M. and Hussaini, M.Y., "Immersed boundary methods for fluid interfaces," in Prosperetti, A. and Tryggvason, G. (Eds.), *Computational Methods for Multiphase Flow*, (2007) Chap. 3 (Cambridge University Press, Cambridge).
- [82] Udaykumar, H.S., Tran, L., Belk, D.M. and Vanden, K.J., "An Eulerian method for computation of multimaterial impact with ENO shock-capturing and sharp interfaces," *J. Comput. Phys.*, **186**, (2003) pp. 136–177.
- [83] Van Hoogstraten, P.A.A., Slaats, P.M.A. and Baaijens, F.P.T., "A Eulerian approach to the finite element modelling of neo-Hookean rubber material," *Appl. Sci. Res.*, **48**, (1991) pp. 193–210.
- [84] Watanabe, H., Sugiura, S., Kafuku, H. and Hisada, T., "Multiphysics simulation of left ventricular filling dynamics using fluid-structure interaction finite element method," *Biophys. J.*, **87**, (2004) pp. 2074–2085.
- [85] Wheeler, A.A., Boettinger, W.J. and McFadden, G.B., "A phase-field model for isothermal phase transitions in binary alloys," *Phys. Rev. A*, **45**, (1992) pp. 7424–7439.
- [86] Xiao, F., Honma, Y. and Kono, T., "A simple algebraic interface capturing scheme using hyperbolic tangent function," *Int. J. Numer. Meth. Fluids*, **48**, (2005) pp. 1023–1040.
- [87] Xiao, F. and Yabe, T., "Computation of complex flows containing rheological bodies," *Comput. Fluid Dyn. J.*, **8**, (1999) pp. 43–49.
- [88] Yokoi, K., Xiao, F., Liu, H. and Fukasaku, K., "Three-dimensional numerical simulation of flows with complex geometries in a regular Cartesian grid and its application to blood flow in cerebral artery with multiple aneurysms," *J. Comput. Phys.*, **202**, (2005) pp. 1–19.
- [89] Youngs, D.L., "Time-dependent multi-material flow with large fluid distortion," in Morton, K.W. and Baines, M.J. (Eds.), *Numerical Methods for Fluid Dynamics*, (1982) pp. 273–285 (Academic Press, New York).
- [90] Yu, Z., "A DLM/FD method for fluid/flexible-body interactions," *J. Comput. Phys.*, **207**, (2005) pp. 1–27.
- [91] Yuki, Y., Takeuchi, S. and Kajishima, T., "Efficient immersed boundary method for strong interaction problem of arbitrary shape object with self-induced flow," *J. Fluid Sci. Tech.*, **2**, (2007) pp. 1–11.
- [92] Zhang, L.T. and Gay, M., "Immersed finite element method for fluid-structure interactions," *J. Fluids and Structures*, **23**, (2007) pp. 839–857.
- [93] Zhang, L.T. and Gay, M., "Imposing rigidity constraints on immersed objects in unsteady fluid flows," *Comput. Mech.*,

42, (2008) pp. 357–370.

- [94] Zhang, L., Gerstenbetger, A., Wang, X. and Liu, W.K., “Immersed finite element method,” *Comput. Methods Appl. Mech. Eng.*, **193**, (2004) pp. 2051–2067.
- [95] Zhang, Q. and Hisada, T., “Analysis of fluid-structure interaction problems with structural buckling and large domain changes by ALE finite element method,” *Comput. Methods Appl. Mech. Eng.*, **190**, (2001) pp. 6341–6357.
- [96] Zhang, Z. and Prosperetti, A., “A second-order method for three-dimensional particle simulation,” *J. Comput. Phys.*, **210**, (2005) pp. 292–324.
- [97] Zhao, H., Freund, J.B. and Moser, R.D., “A fixed-mesh method for incompressible flow-structure systems with finite solid deformation,” *J. Comput. Phys.*, **227**, (2008) pp. 3114–3140.

Appendix A: Finite difference descriptions

1. For mass conservation equation (11) and derivatives of the incremental pressure involved in (31)–(34)

Using the operators in (38), we describe

$$(\nabla \cdot \mathbf{v})_{i,j} = \frac{\delta_i(v_x)|_{i,j}}{\Delta_x} + \frac{\delta_j(v_y)|_{i,j}}{\Delta_y}. \quad (\text{A1})$$

$$(\partial_x \varphi)_{i+\frac{1}{2},j} = \frac{\delta_i(\varphi)|_{i+\frac{1}{2},j}}{\Delta_x}, \quad (\partial_y \varphi)_{i,j+\frac{1}{2}} = \frac{\delta_j(\varphi)|_{i,j+\frac{1}{2}}}{\Delta_y}, \quad (\text{A2})$$

$$\begin{aligned} (\partial_x^2 \varphi)_{i,j} &= \frac{\delta_i(\varphi)|_{i+\frac{1}{2},j} - \delta_i(\varphi)|_{i-\frac{1}{2},j}}{\Delta_x^2}, \quad (\partial_y^2 \varphi)_{i,j} = \frac{\delta_j(\varphi)|_{i,j+\frac{1}{2}} - \delta_j(\varphi)|_{i,j-\frac{1}{2}}}{\Delta_y^2}, \\ (\partial_x \partial_y \varphi)_{i+\frac{1}{2},j+\frac{1}{2}} &= \frac{\varphi_{i+1,j+1} - \varphi_{i,j+1} - \varphi_{i+1,j} + \varphi_{i,j}}{\Delta_x \Delta_y}. \end{aligned} \quad (\text{A3})$$

2. For momentum conservation equation (26)

Here, we show the discretization for each term involved only in the x -momentum equation. The permutations $i \leftrightarrow j$ and $x \leftrightarrow y$ lead to the corresponding discretization in the y -momentum equation. For a quantity q , we here introduce interpolation operators denoted by overlines such as

$$\overline{q}^i|_{i,j} = \frac{q_{i+\frac{1}{2},j} + q_{i-\frac{1}{2},j}}{2}, \quad \overline{q}^j|_{i,j} = \frac{q_{i,j+\frac{1}{2}} + q_{i,j-\frac{1}{2}}}{2}. \quad (\text{A4})$$

The advection terms [38]:

$$\begin{aligned} (v_x \partial_x v_x)_{i+\frac{1}{2},j} &= \frac{\overline{v_x}^i|_{i,j} \delta_i(v_x)|_{i,j} + \overline{v_x}^i|_{i+1,j} \delta_i(v_x)|_{i+1,j}}{2\Delta_x}, \\ (v_y \partial_y v_x)_{i+\frac{1}{2},j} &= \frac{\overline{v_y}^j|_{i+\frac{1}{2},j-\frac{1}{2}} \delta_j(v_x)|_{i+\frac{1}{2},j-\frac{1}{2}} + \overline{v_y}^j|_{i+\frac{1}{2},j+\frac{1}{2}} \delta_j(v_x)|_{i+\frac{1}{2},j+\frac{1}{2}}}{2\Delta_y}. \end{aligned} \quad (\text{A5})$$

The pressure gradient and the divergence of the deviatoric stress tensors:

$$\begin{aligned} (\partial_x \tilde{p})_{i+\frac{1}{2},j} &= \frac{\delta_i(\tilde{p})|_{i+\frac{1}{2},j}}{\Delta_x}, \\ (\partial_x \tilde{\sigma}_{xx})_{i+\frac{1}{2},j} &= \frac{\delta_i(\tilde{\sigma}_{xx})|_{i+\frac{1}{2},j}}{\Delta_x}, \quad (\partial_y \tilde{\sigma}_{xy})_{i+\frac{1}{2},j} = \frac{\delta_j(\tilde{\sigma}_{xy})|_{i+\frac{1}{2},j}}{\Delta_y}, \end{aligned} \quad (\text{A6})$$

where

$$(\tilde{\sigma}_{xx})_{i,j} = 2(\mu_f + (\mu_s - \mu_f)\phi_{s,i,j})L_{xx,i,j} + (\phi_s \tilde{\sigma}_{sh,xx})_{i,j},$$

$$(\tilde{\sigma}_{xy})_{i+\frac{1}{2},j+\frac{1}{2}} = (\mu_f + (\mu_s - \mu_f)\overline{\phi_s}|_{i+\frac{1}{2},j+\frac{1}{2}})(L_{xy,i+\frac{1}{2},j+\frac{1}{2}} + L_{yx,i+\frac{1}{2},j+\frac{1}{2}}) + (\phi_s \tilde{\sigma}_{sh,xy})_{i+\frac{1}{2},j+\frac{1}{2}},$$

$$(\phi_s \tilde{\sigma}_{sh,xx})_{i,j} = \left\{ (2c_1 - 12c_3)\phi_{s,i,j}^{\frac{1}{2}} + (2c_2 + 4c_3)\text{tr}(\tilde{\mathbf{B}})_{i,j} - 2c_2 \tilde{B}_{xx,i,j} \right\} \tilde{B}_{xx,i,j} - 2c_2 \overline{\tilde{B}_{xy}^2}|_{i,j},$$

$$(\phi_s \tilde{\sigma}_{sh,xy})_{i+\frac{1}{2},j+\frac{1}{2}} = \left\{ (2c_1 + 2c_2 - 12c_3)\overline{\phi_s^{\frac{1}{2}}}|_{i+\frac{1}{2},j+\frac{1}{2}} + 4c_3 \overline{\text{tr}(\tilde{\mathbf{B}})}|_{i+\frac{1}{2},j+\frac{1}{2}} \right\} \tilde{B}_{xy,i+\frac{1}{2},j+\frac{1}{2}}.$$

Considering $B_{zz} = 1$, we write the trace of $\tilde{\mathbf{B}}$ as

$$\text{tr}(\tilde{\mathbf{B}})_{i,j} = \tilde{B}_{xx,i,j} + \tilde{B}_{yy,i,j} + \phi_{s,i,j}^{\frac{1}{2}}.$$

3. For the advection terms in (13) and (22)

For a quantity q (corresponding to ϕ_s , \tilde{B}_{xx} , or \tilde{B}_{yy}) defined at the cell centroid (i, j) , we apply the fifth-order WENO scheme [36, 45] to the advection terms in (13) and (22). The advection term $v_x \partial_x q$ is written as

$$(v_x \partial_x q)_{i,j}^{\text{WENO}} = \frac{1}{12\Delta_x} \left\{ \frac{(\bar{v}_x^i|_{i,j} + |\bar{v}_x^i|_{i,j}|)(a_1^{(-)}g_1^{(-)} + a_2^{(-)}g_2^{(-)} + a_3^{(-)}g_3^{(-)})}{a_1^{(-)} + a_2^{(-)} + a_3^{(-)} + \epsilon} + \frac{(\bar{v}_x^i|_{i,j} - |\bar{v}_x^i|_{i,j}|)(a_1^{(+)}g_1^{(+)} + a_2^{(+)}g_2^{(+)} + a_3^{(+)}g_3^{(+)})}{a_1^{(+)} + a_2^{(+)} + a_3^{(+)} + \epsilon} \right\}, \quad (\text{A7})$$

where ϵ is a positive tiny number to avoid division by zero, and

$$a_1^{(\pm)} = (s_2^{(\pm)} s_3^{(\pm)})^2, \quad a_2^{(\pm)} = 6(s_1^{(\pm)} s_3^{(\pm)})^2, \quad a_3^{(\pm)} = 3(s_1^{(\pm)} s_2^{(\pm)})^2,$$

$$\begin{aligned} g_1^{(\pm)} &= 2\delta_i(q)_{i\pm\frac{5}{2},j} - 7\delta_i(q)_{i\pm\frac{3}{2},j} + 11\delta_i(q)_{i\pm\frac{1}{2},j}, \\ g_2^{(\pm)} &= -\delta_i(q)_{i\pm\frac{3}{2},j} + 5\delta_i(q)_{i\pm\frac{1}{2},j} + 2\delta_i(q)_{i\mp\frac{1}{2},j}, \\ g_3^{(\pm)} &= 2\delta_i(q)_{i\pm\frac{1}{2},j} + 5\delta_i(q)_{i\mp\frac{1}{2},j} - \delta_i(q)_{i\mp\frac{3}{2},j}, \end{aligned}$$

$$\begin{aligned} s_1^{(\pm)} &= 13\{\delta_i(q)_{i\pm\frac{5}{2},j} - 2\delta_i(q)_{i\pm\frac{3}{2},j} + \delta_i(q)_{i\pm\frac{1}{2},j}\}^2 \\ &\quad + 3\{\delta_i(q)_{i\pm\frac{5}{2},j} - 4\delta_i(q)_{i\pm\frac{3}{2},j} + 3\delta_i(q)_{i\pm\frac{1}{2},j}\}^2, \\ s_2^{(\pm)} &= 13\{\delta_i(q)_{i\pm\frac{3}{2},j} - 2\delta_i(q)_{i\pm\frac{1}{2},j} + \delta_i(q)_{i\mp\frac{1}{2},j}\}^2 \\ &\quad + 3\{\delta_i(q)_{i\pm\frac{3}{2},j} - \delta_i(q)_{i\mp\frac{1}{2},j}\}^2, \\ s_3^{(\pm)} &= 13\{\delta_i(q)_{i\pm\frac{1}{2},j} - 2\delta_i(q)_{i\mp\frac{1}{2},j} + \delta_i(q)_{i\mp\frac{3}{2},j}\}^2 \\ &\quad + 3\{3\delta_i(q)_{i\pm\frac{1}{2},j} - 4\delta_i(q)_{i\mp\frac{1}{2},j} + \delta_i(q)_{i\mp\frac{3}{2},j}\}^2, \end{aligned}$$

Likewise, $(v_y \partial_y q)_{i,j}^{\text{WENO}}$ is computed using the interpolated advection velocity $\bar{v}_y^j|_{i,j}$. For \tilde{B}_{xy} defined at the cell apex $(i + \frac{1}{2}, j + \frac{1}{2})$, using the interpolated velocities $\bar{v}_x^j|_{i+\frac{1}{2},j+\frac{1}{2}}$ and $\bar{v}_y^i|_{i+\frac{1}{2},j+\frac{1}{2}}$, we evaluate $\mathbf{v} \cdot \nabla \tilde{B}_{xy}$ in a similar manner.

Appendix B: Spectral algorithm to find sharp interface solution for the parallel layers problem

We here explain the sharp interface approach to solve the one-dimensional fluid-structure coupling problem by means of (pseudo) spectral method. We obtain accurate solutions, which are used for validating the present full Eulerian model by comparisons.

Due to the symmetry of the system with respect to $y = 0$ illustrated in figure 5, we consider the upper half region $y \geq 0$ and write the fluid and solid velocities v_f , v_s in a Fourier series form

$$v_f(\tilde{y}, t) = V_I(t) + \frac{\tilde{y}}{L_f}(V_W(t) - V_I(t)) + \sum_{k=1}^{\infty} v_{f,k}(t) \sin \frac{\pi k \tilde{y}}{L_f}, \quad (\text{B1})$$

$$v_s(y, t) = \frac{V_I(t)y}{L_s} + \sum_{k=1}^{\infty} v_{s,k}(t) \sin \frac{\pi k y}{L_s}, \quad (\text{B2})$$

where V_I is the velocity at the fluid-structure interface ($y = L_s$), V_W is the given velocity of the upper wall, $v_{f,k}$ and $v_{s,k}$ are expansion coefficients, and $\tilde{y} = y - L_s$. The expressions (B1) and (B2) satisfy the continuity of the velocity ($v_f = v_s$) at the interface $y = L_s$, the no-slip condition ($v_f = V_W$) on the upper wall $y = L_s + L_f$, and the symmetric condition ($v_s = 0$) at $y = 0$. From (B2), we readily find the solid displacement u_s as

$$u_s(y, t) = \frac{U_I(t)y}{L_s} + \sum_{k=1}^{\infty} u_{s,k}(t) \sin \frac{\pi k y}{L_s}, \quad (\text{B3})$$

where U_I and $u_{s,k}$ yield

$$\frac{dU_I}{dt} = V_I, \quad \frac{du_{s,k}}{dt} = v_{s,k}. \quad (\text{B4})$$

From the momentum equations (2), with the stress expressions (10) and (17), we obtain

$$\frac{dV_I}{dt} + \frac{\tilde{y}}{L_f} \left(\frac{dV_W}{dt} - \frac{dV_I}{dt} \right) + \sum_{k=1}^{\infty} \left\{ \frac{dv_{f,k}}{dt} + \frac{\mu_f}{\rho} \left(\frac{\pi k}{L_f} \right)^2 v_{f,k} \right\} \sin \frac{\pi k \tilde{y}}{L_f} = 0, \quad (\text{B5})$$

$$\frac{y}{L_s} \frac{dV_I}{dt} + \sum_{k=1}^{\infty} \left\{ \frac{d^2 u_{s,k}}{dt^2} + \frac{2(c_1 + c_2)}{\rho} \left(\frac{\pi k}{L_s} \right)^2 u_{s,k} + \frac{\pi k}{\rho L_s} \sigma_{\text{NL},k} \right\} \sin \frac{\pi k y}{L_s} = 0, \quad (\text{B6})$$

where σ_{NL} denotes the nonlinear contribution in the solid stress with respect to the displacement. The definition of σ_{NL} and the relation with the expansion coefficients $\sigma_{\text{NL},k}$ are

$$\sigma_{\text{NL}} \equiv 4c_3 \left(\frac{\partial u_s}{\partial y} \right)^3 = \sum_{k=0}^{\infty} \sigma_{\text{NL},k} \cos \frac{\pi k y}{L_s}. \quad (\text{B7})$$

From the orthogonality in the sine function, (B5) and (B6) are reduced to the modal relations

$$\frac{2}{\pi k} \left\{ \frac{dV_I}{dt} - (-1)^k \frac{dV_W}{dt} \right\} + \frac{dv_{f,k}}{dt} + \frac{\mu_f}{\rho} \left(\frac{\pi k}{L_f} \right)^2 v_{f,k} = 0, \quad (\text{B8})$$

$$-\frac{2(-1)^k}{\pi k} \frac{dV_I}{dt} + \frac{d^2 u_{s,k}}{dt^2} + \frac{2(c_1 + c_2)}{\rho} \left(\frac{\pi k}{L_s} \right)^2 u_{s,k} + \frac{\pi k}{\rho L_s} \sigma_{\text{NL},k} = 0, \quad (\text{B9})$$

for $1 \leq k < \infty$. The continuity of the shear stress at the interface $y = L_s$ is

$$\begin{aligned} & \frac{\mu_f(V_W - V_I)}{L_f} - \frac{2(c_1 + c_2)U_I}{L_s} - \sigma_{\text{NL},0} \\ & + \sum_{k=1}^{\infty} \left[\frac{\mu_f \pi k v_{f,k}}{L_f} - (-1)^k \left\{ \frac{2(c_1 + c_2) \pi k u_{s,k}}{L_s} + \sigma_{\text{NL},k} \right\} \right] = 0. \end{aligned} \quad (\text{B10})$$

The equation set to be solved consists of (B7)–(B10). In the numerical determination of the coefficients $v_{f,k}$, $u_{s,k}$, V_I and U_I , we truncate the number of the modes appeared in the infinite series summation of (B10) up to $k = K - 1$. If K is chosen as an integer power of 2, the fast Fourier sine transform can be applied to efficiently evaluating v_f and u_s

respectively given in (B1) and (B3), and the fast Fourier cosine transforms determine the nonlinear part of the solid stress in a pseudo-spectral way

$$\sigma_{\text{NL},k} \approx \frac{8c_3}{N(1+\delta_{k0})} \sum_{j=0}^{K-1} \left\{ \frac{U_I}{L_s} + \sum_{l=0}^{K-1} \frac{\pi n u_{s,l}}{L_s} \cos \frac{\pi l(j+\frac{1}{2})}{K} \right\}^3 \cos \frac{\pi k(j+\frac{1}{2})}{K}, \quad (\text{B11})$$

where δ is the Kronecker delta.

In the case of $c_3 = 0$ (the linear Mooney-Rivlin material), the system is linear since σ_{NL} vanishes. Considering the wall velocity is $V_W(t) = \text{Im}(\hat{V}_W \exp(i\omega t))$, we may apply the separation of variable to the velocities and the displacement

$$\begin{aligned} V_I(t) &= \text{Im}(\hat{V}_I \exp(i\omega t)), \\ v_{f,k}(t) &= \text{Im}(\hat{v}_{f,k} \exp(i\omega t)), \\ u_{s,k}(t) &= \text{Im}(\hat{u}_{s,k} \exp(i\omega t)), \end{aligned} \quad (\text{B12})$$

which reduce the differential equations (B8) and (B9) with respect to t into the algebraic ones. We readily find the expansion coefficients

$$\hat{v}_{f,k} = \frac{\{(-1)^k \hat{V}_W - \hat{V}_I\} \alpha_k}{\pi k}, \quad (\text{B13})$$

$$\hat{u}_{s,k} = \frac{i(-1)^k \hat{V}_I \beta_k}{\pi \omega k}, \quad (\text{B14})$$

$$\hat{V}_I = \frac{\frac{\mu_f \hat{V}_W}{L_f} \left(1 + \sum_{k=1}^{K-1} (-1)^k \alpha_k \right)}{\frac{\mu_f}{L_f} \left(1 + \sum_{k=1}^{K-1} \alpha_k \right) + \frac{2(c_1 + c_2)}{i\omega L_s} \left(1 - \sum_{k=1}^{K-1} \beta_k \right)}, \quad (\text{B15})$$

where

$$\alpha_k = \frac{2i\omega}{\frac{\mu_f \pi^2 k^2}{\rho L_f^2} + i\omega}, \quad \beta_k = \frac{2\omega^2}{\frac{2(c_1 + c_2) \pi^2 k^2}{\rho L_s^2} - \omega^2}.$$

In the case of $c_3 \neq 0$ (e.g., the incompressible Saint Venant-Kirchhoff material), the system is nonlinear since $\sigma_{\text{NL}} \neq 0$, and thus the numerical time integration is needed. Here, it is carried out using the second-order Adams-Bashforth and Crank-Nicolson schemes. We here put an superscript (n) to a quantity to indicate the n -th time level ($t = n(\Delta t)$). If all the variables at the n -th and $(n-1)$ -th time levels are known, together with the prescribed wall velocity

$$V_W^{(n+1)} \equiv V_W((n+1)(\Delta t)) = \text{Im}(\hat{V}_W \exp(i\omega(n+1)(\Delta t))),$$

we update U_I , $v_{f,k}$, $u_{s,k}$, and V_I at the $(n+1)$ -th time level:

$$U_I^{(n+1)} = U_I^{(n)} + \frac{(\Delta t)}{2} (V_I^{(n+1)} + V_I^{(n)}), \quad (\text{B16})$$

$$v_{f,k}^{(n+1)} = \frac{E_{vf,k}}{1 + \frac{(\Delta t) \mu_f \pi^2 k^2}{2\rho L_f^2}}, \quad (\text{B17})$$

$$\begin{aligned} u_{s,k}^{(n+1)} &= \frac{(-1)^k (\Delta t) (V_I^{(n+1)} - V_I^{(n-1)})}{\pi k} + 2u_{s,k}^{(n)} - u_{s,k}^{(n-1)} \\ &\quad - (\Delta t)^2 \left(\frac{2(c_1 + c_2) \pi^2 k^2}{\rho L_s^2} u_{s,k}^{(n)} + \frac{\pi k}{\rho L_s} \sigma_{\text{NL},k}^{(n)} \right), \end{aligned} \quad (\text{B18})$$

$$V_I^{(n+1)} = \frac{E_{VI}}{\frac{\mu_f}{L_f} + \left(N - \frac{1}{2}\right) \frac{(c_1 + c_2)(\Delta t)}{L_s} + \sum_{k=0}^{K-1} \frac{4\rho\mu_f L_f}{2\rho L_f^2 + (\Delta t)\mu_f \pi^2 k^2}}, \quad (\text{B19})$$

where

$$\begin{aligned} E_{vf,k} &= \left(1 - \frac{(\Delta t)\mu_f \pi^2 k^2}{2\rho L_f^2}\right) v_{f,k}^{(n)} - \frac{2\{V_I^{(n+1)} - V_I^{(n)} - (-1)^k \delta V_W\}}{\pi k}, \\ E_{VI} &= \frac{\mu_f V_W^{(n+1)}}{L_f} - \frac{(c_1 + c_2)\{2U_I^{(n)} + (\Delta t)V_I^{(n)}\}}{L_s} - 2\sigma_{\text{NL},0}^{(n)} + \sigma_{\text{NL},0}^{(n-1)} \\ &+ \sum_{k=1}^{K-1} \left[\frac{\mu_f}{L_f} \left\{ \frac{\pi k \{2\rho L_f^2 - (\Delta t)\mu_f \pi^2 n^2\} v_{f,n}^N + 4\rho L_f^2 \{V_I^{(n)} + (-1)^k \delta V_W\}}{2\rho L_f^2 + (\Delta t)\mu_f \pi^2 n^2} \right\} \right. \\ &+ \frac{2(c_1 + c_2)}{L_s} \left\{ (\Delta t)V_I^{(n-1)} + (-1)^k \pi k \left(\gamma_k u_{s,k}^{(n)} + u_{s,k}^{(n-1)} \right) \right\} \\ &\left. + (-1)^k \left(\gamma_k \sigma_{\text{NL},k}^{(n)} + \sigma_{\text{NL},k}^{(n-1)} \right) \right], \end{aligned}$$

$$\delta V_W = V_W^{(n+1)} - V_W^{(n)}, \quad \gamma_k = \frac{2(c_1 + c_2)(\Delta t)^2 \pi^2 k^2}{\rho L_s^2} - 2.$$

After a sufficiently long computation, we obtain temporally periodic solutions.

We checked the convergence of the solution as a function of the truncated mode K . We confirmed that within the parameter range shown in figure 9, the results with $K = 2048$ are accurate enough to be regarded as the reference solutions for comparison.